Doctoral Thesis

Optically Pumped Lasing and Electroluminescence Properties of Single-crystal Lead Halide Perovskites Prepared by Cast-capping Method

(キャスト - キャッピング法により作製したハロゲン化鉛ペロブスカイト単結晶の光励起レージングと電界発光特性)

Van-Cao Nguyen

March 2018

Graduate School of Materials Science

Nara Institute of Science and Technology

Table of Contents

Abstract

Over past a few years, organic-inorganic perovskites have received extraordinary research community attention since the performance of devices using perovskites achieved up to above 20% light harvest efficiency and 10% external quantum efficiency for solar cells and light-emitting diodes, respectively. Not only their unique physical properties such as direct bandgap, high optical absorption, tunable wavelengths but also solution-processed low-cost fabrication led to a new generation of applications in their photovoltaic and optoelectronic devices. Conventionally, the spin-coating method has been used as a low-cost process to fabricate perovskite thin films. However, on demand of high-quality crystalline perovskites, a high-cost method, for example physical vapor deposition (PVD) of PbX_2 and MAX (where MA = CH_3NH_3, X = Cl, Br or I), is also widely used. Towards further progress hereafter, in particular, for practical device applications, there is a demand to improve the growth method which allows a control of crystal size and thickness as well as polymorphic stability. In my thesis, a simply modified solution process, namely "cast-capping" method, was developed affording to grow all kinds of perovskite crystals between various substrates. Consequently, the optically pumped lasing and electroluminescence of $MAPbX_3$ were investigated in thin large-sized single crystals.

In Chapter 1, the history of rapid development with improving performances in applications using perovskites is introduced. Then, their unconventional electronic properties through the structure-properties relationship are discussed.

In Chapter 2, the cast-capping method is presented to prepare single crystal perovskites. All kind of methylammonium lead halide perovskites $MAPbX_3$ and their mixture ($MAPbCl_xBr_y$ and $MAPbBr_xI_y$, where $x + y = 3$) were crystallized by this method. It was found that the orientation of crystals depended on the substrates: the (100) planes of cubic $MAPbBr_3$ were grown when ITO substrates were used in contrast to the (110) planes when glass substrates were used. The kind of halogens also affected the growth direction. When glass substrates were used, the (100) planes of both cubic $MAPbI_3$ and $MAPbCl_3$ crystals grew two-dimensionally between the top and bottom substrates, contrastingly to the cubic $MAPbBr_3$ crystal in which the (110) planes grew in contact with the substrates. For the mixture perovskites, cubic crystals with color-tunable photoluminescence (PL) were obtained depending on the halogen ratio in the precursor solution.

In Chapter 3, both one-dimensional strip-shaped and two-dimensional slab-shaped crystals were obtained depending on the growth manner in the cast-capping methods. In the former crystal, edge-emitting lasing based on Fabry-Pérot resonation was observed under optical pumping with a pulsed excitation. On the other side, the latter crystal grown between distributed Bragg reflector (DBR) mirrors exhibited surface-emitting laser. The lower lasing threshold (12 $\mu J/cm^2$) and higher Q factor (1470) were obtained for the edge-

emitting laser owing to well-shaped side facets of the strip-shaped crystal whereas the inhomogeneous thickness of the slab-shaped crystal resulted in inferior cavity quality.

In Chapter 4, a simple light-emitting diode with ITO/$MAPbBr_3$/ITO structure was fabricated by the cast-capping method. Because there is no effect of transport layers, intrinsic electroluminescence (EL) of the single-crystal perovskites could be characterized. Under application of bias voltages above 2 V, the device showed blinking EL at the crystal edges and its emission peak was red-shifted by 0.02 eV as compared to PL. It suggests that the injected carriers are diffused and accumulated at the crystal edges, then generate excitons. Subsequently, the excitons may be trapped in the radiative sub-gap states to emit photons or quenched through non-radiative recombination by carrier traps concentrated at crystal edges.

Chapter 5 summarized this study presenting the cast-capping method to prepare large-size and high-quality single-crystal perovskites. The formation of crystals depended on the surface properties and halogen compositions. Under optical pumping, edge- and surface-emitting lasers were achieved for strip- and slab-shaped crystals, respectively. Finally, the simple ITO/$MAPbBr_3$/ITO device exhibited unique blinking EL which leads to deeper understanding of emission mechanism in single-crystal perovskites.

Chapter 1
Introduction

Organic-inorganic halide perovskite semiconductors are an emerging class of materials that have led to a great performance of low-cost optoelectronic devices, which is approaching the theoretical limits and comparable with high-cost inorganic semiconductor devices. Their interesting properties such as long diffusion length, solution processability and wavelength tunability across near-UV to near-infrared (IR) through its halide stoichiometry, have made this material promising in application to solar cells and emitting devices. A variety of growth methods and film formation processes have been developed to promote the availability of perovskites for photovoltaics, light-emitting diodes (LEDs), lasing devices, and host of other major optoelectronic applications.

In this chapter, first these backgrounds of perovskite researches are introduced, then, their crystal structures and thin film preparation methods are described. Finally, the aim of this work is stated.

1.1 Backgrounds

Calcium Titanium Oxide mineral ($CaTiO_3$) found in 1839 by Gustav Rose in the Ural Mountains, Russia, is named 'perovskite' following a Russian mineralogist Lev Perovski. Since 2009, organic-inorganic lead halide perovskite compounds $MAPbBr_3$ and $MAPbI_3$ (where MA = CH_3NH_3) were initially used as visible-light sensitizers in photoelectrochemical cells[1]. At that time, the efficiency of perovskite-based cells was achieved to be 3.81%. After 3 years, Hui-Seon Kim et al. reported exceeding 9% for solar cells using $MAPbI_3$[2]. The authors has also indicated that the stability is up to 500 hours at room temperature without encapsulation. Surprisingly, the efficiency of ~18% was achieved with millimeter crystalline grains of $MAPbI_3$ in planar solar cells.[3] Beside the high efficiency, a study by C. Gerbaldi group indicated a long term stability (tested for 6 months) for perovskite solar cells with a photocurable fluoropolymer.[4] Up to now, there are thousands papers have been published to reduce the fabrication cost and improve the efficiency of devices.[5] The history of solar cells based on perovskites has been summarized as shown in Fig. 1.1.1.

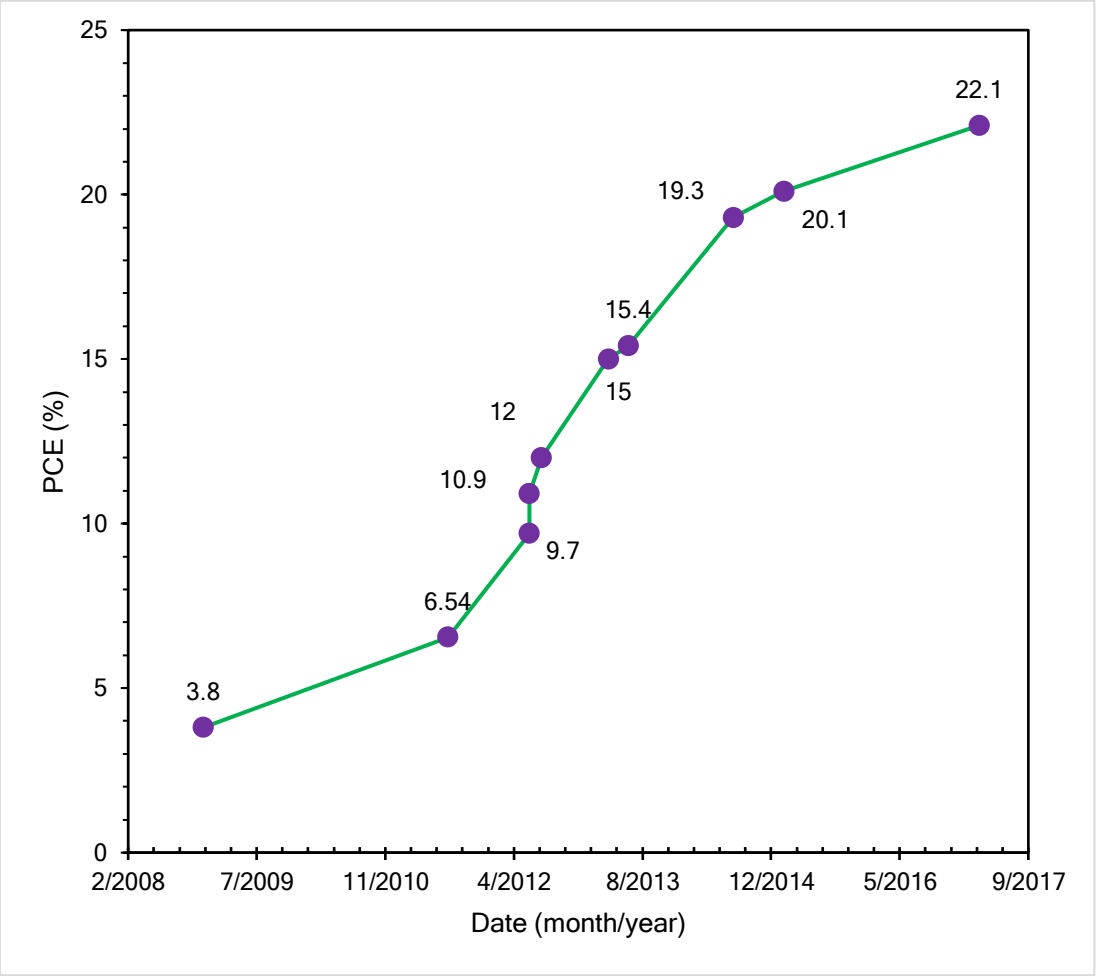

Fig. 1.1.1: *Progress in perovskite solar cell efficiency.*[1,2,6–13]

Not only applied in harvesting light but also perovskites are interesting in lasing and LEDs.[5,14] The sharp optical absorption and large carrier mobilities in perovskites suggest a valuable applicability to LEDs that can achieve high brightness at low driving voltages. Following the increasing efficiency in solar cell, the external quantum efficiency (EQE) depends on the improvement of fabrication methods as summarized in Fig. 1.1.2. In 2014, the LED using $MAPbBr_3$ as an emitting layer achieved just EQE of 0.1%.[15] However, the EQE was increased up to 8.53% when T. W. Lee et al. reduced the grain size of $MAPbBr_3$

crystal below 100 nm.[16] Similar to this architectural fabrication, the EQE of the LED approached 9.3% by adding a long chain halide to the precursor solution before spin-coating perovskite thin films. The authors also indicated very long shelf stability of these devices more than 3 months.

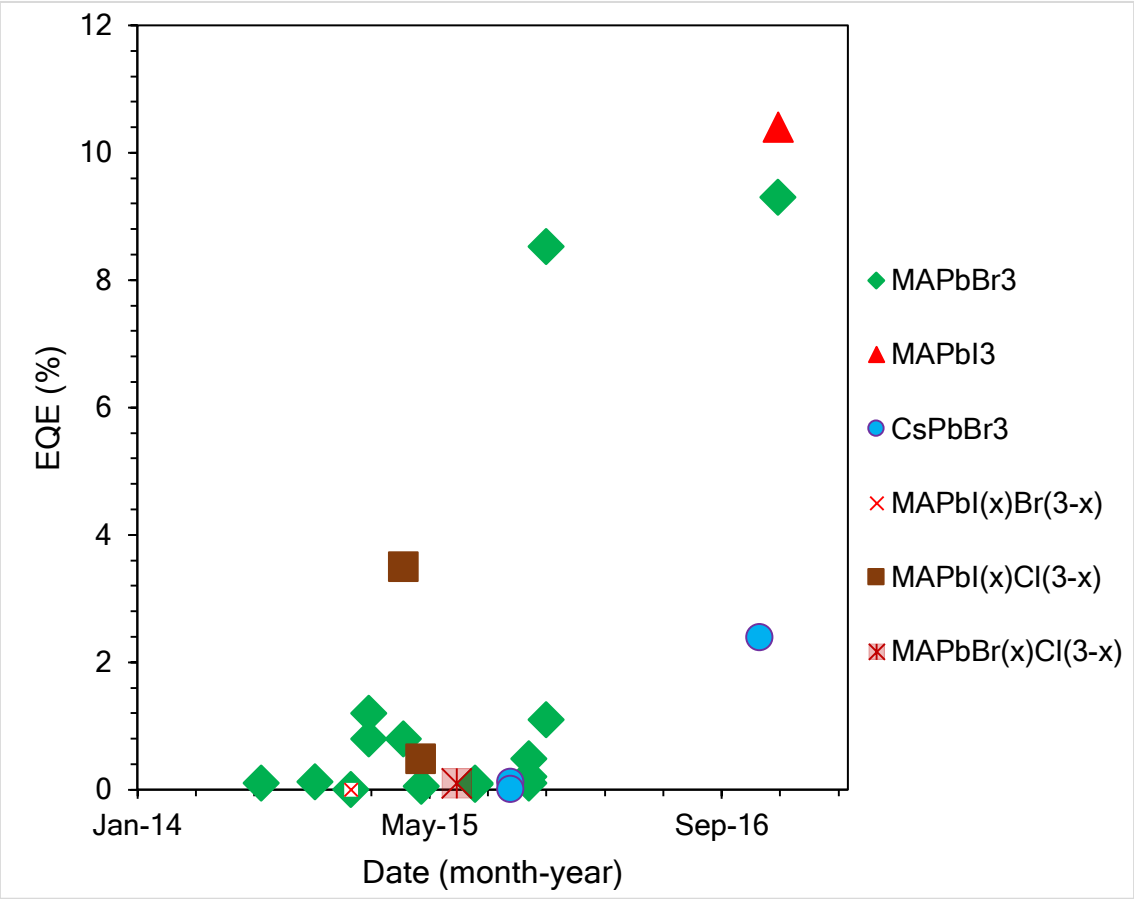

Fig. 1.1.2: *Overview of EQE for lead halide perovskites in LEDs.*

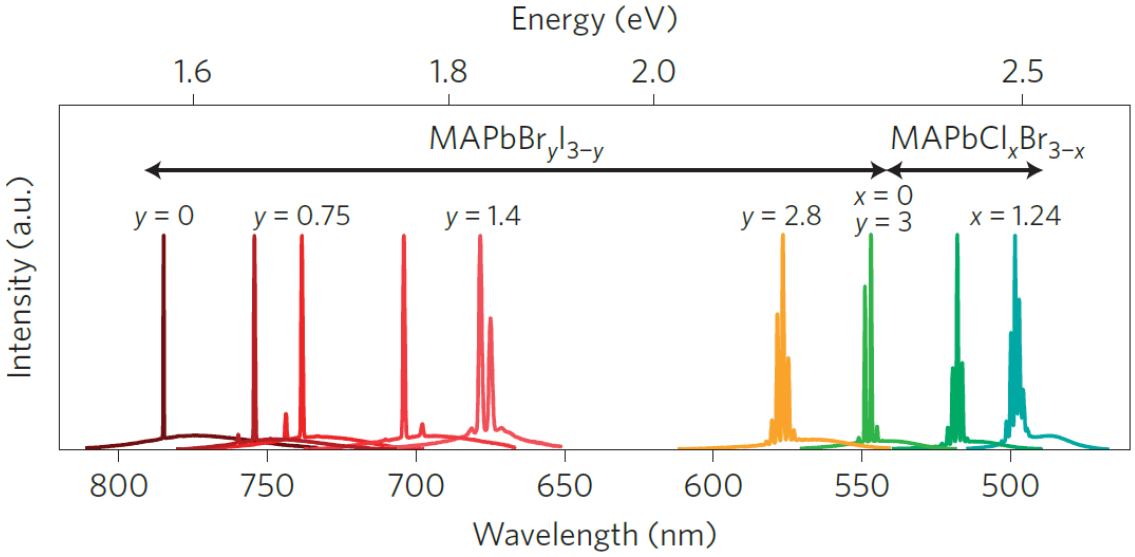

Fig. 1.1.3: *Tunable lasing emission wavelength from mixed lead halide perovskites.*[17] Reproduced with permission from H. Zhu et al. *Nat. Mater.* **14**, 636-642 (2015), Copyright Springer Nature, Macmillan Publishers Limited.

In addition, the band-gap of perovskites can be easily tuned by simple substitution of metal cations, inorganic anions, or organic ligands.[18–20] Here, this study just focus on the halide-based color-tuning, which is widely used in optoelectronic devices. The $MAPbCl_xBr_{3-x}$ and $MAPbBr_yI_{3-y}$ with various stoichiometry were successfully synthesized by controlling the mixing amount of methylammonium halide in the precursor solution.[17] H. Zhu at al. observed the tunable lasing emission wavelengths from these mixture perovskites at room temperature as shown in Fig. 1.1.3. These unique tunable bandgaps were also applied to fabricate multicolored LEDs.[15,18] The

electroluminescence from near-UV to near-IR was achieved by Y. H. Kim et al. as shown in Fig. 1.1.4.

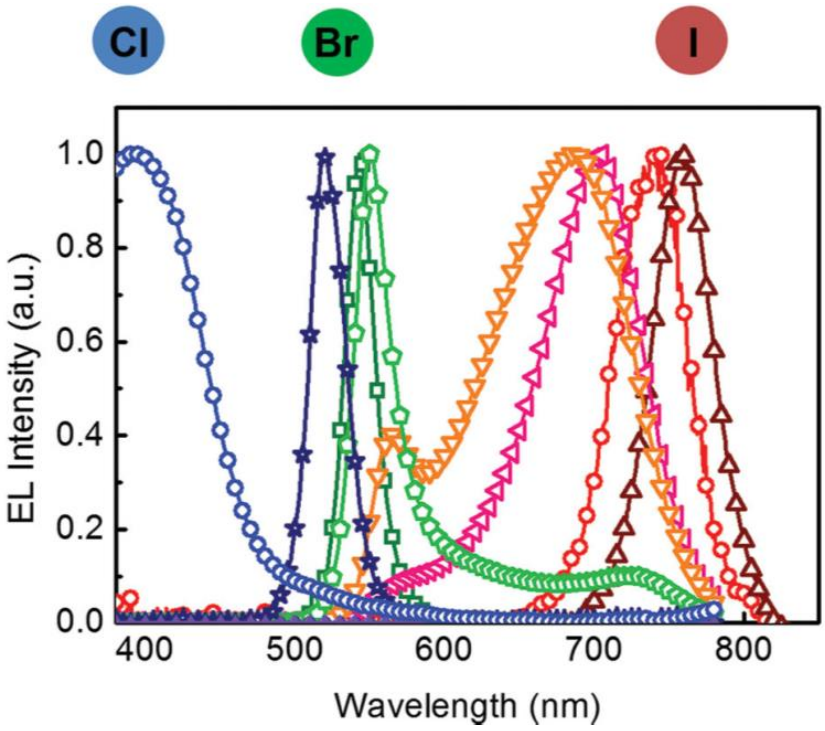

Fig. 1.1.4: *Electroluminescence of mixed perovskites LEDs.*[18] Reproduced with permission. Copyright 2014, Wiley-VCH.

1.2 Crystal structure

One of most useful perovskite is organic-inorganic hybrid perovskites based on ABX_3 structure.[21,22] It is characterized by $[BX_6]^{4-}$ octahedral which sharing corners in all three orthogonal directions to generate an infinite 3-dimentional (3D) $[BX_3]^-$ framework as shown in Fig. 1.2.1. Typically, the "A" cation is methylammonium (MA), formamidinium (FA) etc., while "B" is metal (Pb, Sn, Ge …) and X is halogen (Cl, Br and I). The rules that govern the perovskite formation were tackled by Goldschmidt's Tolerance Factor concept:

$$t = (r_A + r_X)/\sqrt{2}(r_B + r_X) \qquad (1)$$

where r_A, r_B and r_X are the ionic radii for the corresponding ions and the t is tolerance factor in the ABX_3 formula. For most cubic perovskite structures, the tolerance value $0.8 \leq t \leq 0.9$.[12,14,15]

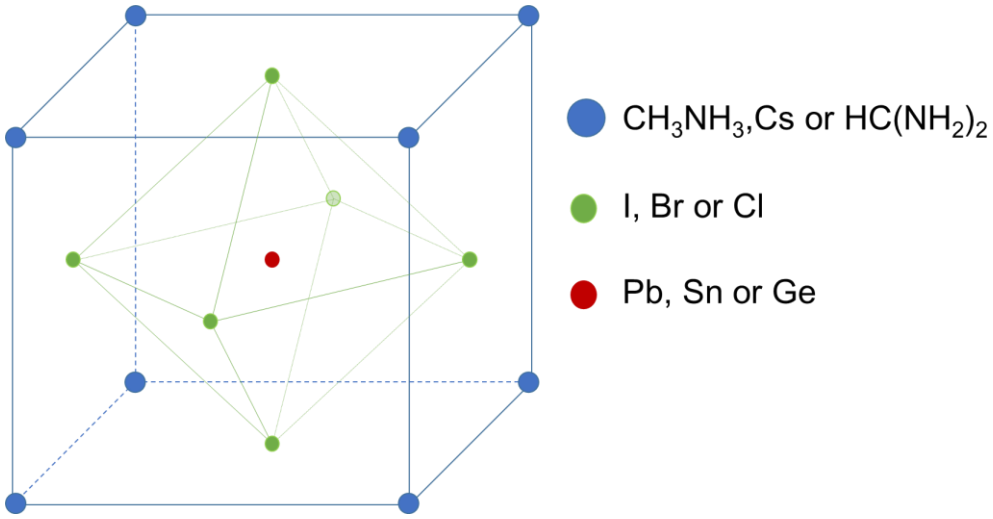

Fig. 1.2.1: *Crystal structure of organic-inorganic halide perovskites.*

Based on these consideration, the most common 3D perovskite crystal structure is lead methylammonium trihalide perovskites $MAPbX_3$ (where X = Cl, Br or I). For this compound, the cubic lattice constants vary from 5.66 Å (X = Cl), 5.90 Å (X = Br) and 6.33 Å (X = I). In fact, the methylammonium cation undergoes rapid isotropic reorientation. Upon cooling, the structures distort to lower symmetry as the motion of the methylammonium cation becomes more restricted (table 1.2.1).[23] As a result, the crystal system becomes cubic in the case of $MAPbCl_3$ and $MAPbBr_3$, but tetragonal in the case of $MAPbI_3$ at room temperature. Noteworthy, in contrast with this theory, the cubic-structure $MAPbI_3$ crystals can be stable at room temperature in bulk crystals[24] or confined by TiO_2 with the aid of chlorine.[25]

Table 1.2.1: *Transition phases of $MAPbX_3$ crystals depending on temperature.*

$MAPbX_3$	**Temperature (K)**	**Crystal system**	**Space group**
Cl	> 178.8	Cubic	*Pm3m*
	172.9 ~ 178.8	Tetragonal	*P4/mmm*
	< 172.9	Orthorhombic	$P222_1$
Br	> 236.9	Cubic	*Pm3m*
	155.1 ~ 236.9	Tetragonal	*I4/mcm*
	149.5 ~ 155.1	Tetragonal	*P4/mmm*
	< 149.5	Orthorhombic	$Pna2_1$
I	> 327.4	Cubic	*Pm3m*
	162.2 ~ 327.4	Tetragonal	*I4/mcm*
	< 162.2	Orthorhombic	$Pna2_1$

1.3 Fabrication method

1.3.1 Spin-coating method

One of most interesting properties of perovskites for optoelectronic and optics devices is their low-cost fabrication processability. Until now, as a simple and convenient process to make thin film perovskites, spin-coating has been widely used.[9,11,19,20,21] Typically, methylammonium halide and lead halide are dissolved in a polar solvent such as N, N-dimethylformamide (DMF) and/or dimethyl sulfoxide (DMSO). Then, the precursor solution is dropped and spread on the substrate at an appropriate rotation speed (Fig. 1.3.1a). Conventionally, the mixture ratio of MAX is higher than the stoichiometrical 1:1 of MAX:PbX_2 to form $MAPbX_3$ crystalline. These exceed amount of methylammonium halide is evaporated by thermal annealing after spin-coating. Noteworthy, T. W. Lee et al. indicated that the perovskite crystal size depended on MAX:PbX_2 ratio.[16] In that study, the smallest grain size is below 100 nm when MAX:PbX_2 = 1.05:1. Another study by B. P. Rand also used addition of long-chain ammonium halides in the precursor solution to reduce perovskite grain size.[27] To improve the uniformity of the thin film, a highly volatile nonpolar solvent such as chloroform or toluene was used which induced fast crystallization.[9, 20]

Another alternative technique was employed in spin-coating method, namely two-

step coating.[9,29–32] At first, MAX and PbX_2 are dissolved in 2-propanol and DMF, respectively. Similar to the spin-coating process described above, PbX_2 is spin-coated on substrate (first step), then MAX is spin-coated on PbX_2 thin layer or the PbX_2 substrate is dipped in the MAX solution. Consequently, the $MAPbX_3$ thin film is formed on the substrate (Fig. 1.3.1b). Note that in the present study, $MAPbX_3$ thin film was prepared by dipping the spin-coated PbX_2 on solution of MAX in 2-propanol.

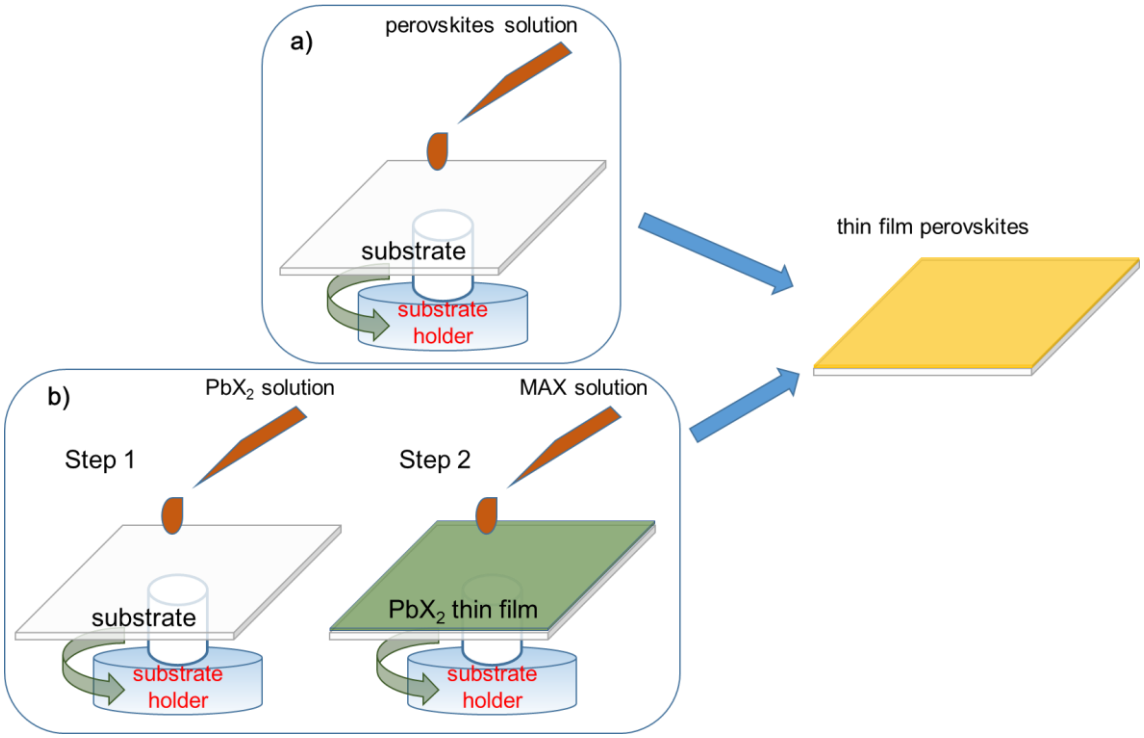

Fig. 1.3.1: *Schematic of spin-coating method: a) one step and b) two-step spin-coating.*

1.3.2 Chemical/physical vapor deposition

The spin-coating method maintains some drawbacks such as limited substrate materials and inhomogeneous morphology which result in low performance of LEDs or low efficiency in solar cells. As an alternative method, chemical/physical vapor deposition has also been widely used to synthesize high-quality crystalline perovskite films. Generally, the inorganic and organic sources are vaporized at high temperature in a vacuum and perovskites are deposited on the substrates as shown in Fig. 1.3.2. In 2014, Q. Xiong et al. successfully fabricated nano-platelets on muscovite mica substrates.[33,34] First, they heat up the inorganic source at high temperature (380°C for PbI_2, 350°C for $PbBr_2$ and 510°C for $PbCl_2$) in quartz tube flowed with Ar and H_2 gas. The lead halide platelets is deposited on the muscovite mica substrate. Then, nano-platelet perovskites are formed by a gas-solid hetero-phase reaction with methylammonium halide molecules.

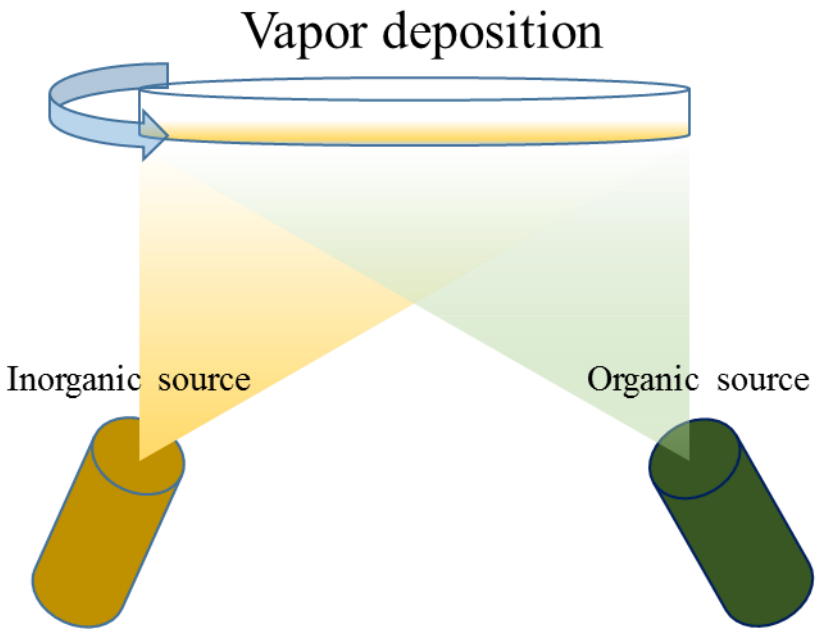

Fig. 1.3.2: *Schematic of vapor deposition method.*

1.3.3 Other methods

a) Nanowire fabrication

One dimensional (1D) nanostructured semiconductors have been exhibiting excellent performance in nanoelectronics, photoelectronics because of highly localized coherent output, and efficient wave-guiding. In 2015, X-Y. Zhu et al. grew high-quality single-crystal nanowires by low-temperature processing.[17] Firstly, they drop-casted 100 mg/mL $PbAc_2 \cdot 3H_2O$ aqueous solution on a hot glass substrate in an oven at 65ºC and dried for 30 min. Then, nanowires of $MAPbX_3$ perovskite were surface-initiated grown from $PbAc_2$ when the $PbAc_2$ thin film was dipped in high concentration of MAX solution in 2-propanol (MAX/IPA) at room temperature.

As soon as the $PbAc_2$ was placed in MAX/IPA solution, the $MAPbX_3$ film was immediately formed on the $PbAc_2$ surface following the reaction:

$$PbAc_2 \text{ (solid)} + CH_3NH_3^+ \text{ (solution)} + X^- \text{ (solution)} \rightarrow CH_3NH_3PbX_3 \text{ (solid)}$$

This $MAPbX_3$ film not only serves as a seed to initiate the crystal growth, but also plays a key role in maintaining a relative low supersaturation condition for nanowire growth. Noteworthy, the formation of soluble complex ion PbX_4^{2-} in IPA becomes thermodynamically favorable due to high concentration of MAX. The unconverted $PbAc_2$ is slowly dissolved into the solution until PbX_4^{2-} reaches the equilibrium point for precipitation with MA^+ and finally reaches the supersaturation to be crystallized into $MAPbX_3$. The growth mechanism is described by the following two-step reactions:

$$PbAc_2 \text{ (solid)} + 4X^- \text{ (solution)} \rightarrow PbX_4^{2-} \text{ (solution)} + 2Ac^- \text{ (solution)}$$

$$PbX_4^{2-} \text{ (solution)} + CH_3NH_3^+ \text{ (solution)} \rightarrow CH_3NH_3PbX_3 \text{ (solid)} + X^- \text{ (solution)}$$

As a result, high-quality nanowires of $MAPbX_3$ were grown as shown in Fig. 1.3.3. In this study, room-temperature nanowire lasing with very low lasing was achieved at low excitation threshold (220 nJ/cm^2 for $MAPbI_3$ and 300 nJ/cm^2 for $MAPbBr_3$) with high Q

factor up to 3,600 for $MAPbI_3$ and 2,360 for $MAPbBr_3$. Noteworthy, the wavelength-tunable lasing was also achieved when they simply mix different amounts of MAI and MABr or MABr and MACl in the precursor solution.

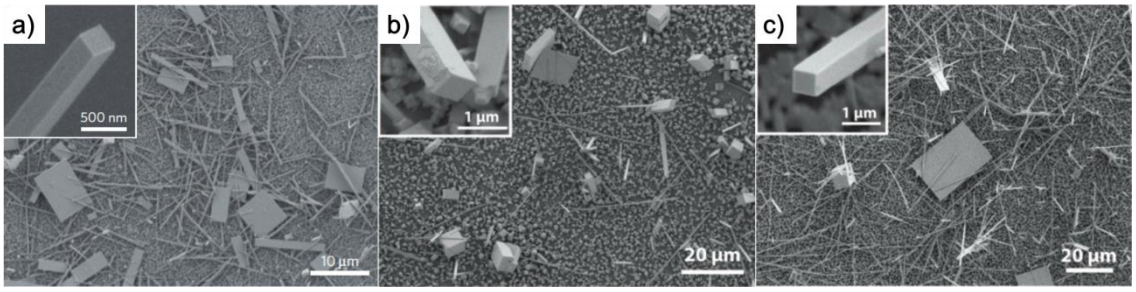

Fig. 1.3.3: *SEM images of a) $MAPbI_3$, b) $MAPbBr_3$, and $MAPbCl_3$ nanowires.*[17] Reproduced with permission from H. Zhu et al. *Nat. Mater.* **14**, 636-642 (2015), Copyright Springer Nature, Macmillan Publishers Limited.

The nanorods were also used for light-emitting devices by P. Yang et al.[35] Surprisingly, they found that $MAPbBr_3$ nanorods were conversed to $MAPbI_3$ through the anion exchange by MAI vapor at 140°C. Because the operation voltage of these devices is high (around 3.5V) and the external quantum efficiency is not mentioned, it suggests that nanorods thin film structure is not suitable for high performance light-emitting devices. However, single nanowire is extremely promising for electrically excited lasing owing to their high-quality gain medium, low-trap state density and cavity quality with well-shaped edge facets of nanowire crystals.[14]

b) Bulk-crystal fabrication

To apply for optoelectronic devices, low-dimensional perovskites are widely used. However, three-dimensional (3D) perovskites are extensively synthesized to investigate the fundamental properties of this kind of materials. All of methods such as anti-solvent vapor-assisted crystallization, seed solution-growth method, cooling-induced crystallization, and inverse temperature crystallization apparatus start from an initial $MAPbX_3$. The $MAPbX_3$ is saturated in high concentration perovskites solution to precipitate seeds which grow 3-dimensionally to form large size bulk crystals as shown in Fig 1.3.4.[36] Surprisingly, by using mixed chlorobenzene/γ-butyrolactone to dissolve MAI:PbI_2 and keeping at 60°C, stable cubic crystals were formed at room temperature. By mixing the precursor methylammonium halide, the single-crystal mixed perovskites were also obtained. Very low trap-state density and long carrier diffusion length of perovskites were confirmed in the bulk crystals, and the narrowband photodectectors with single-crystal perovskites was investigated.[37] That study prospects new applications of perovskites for selected-wavelength imaging and flame detection.[38]

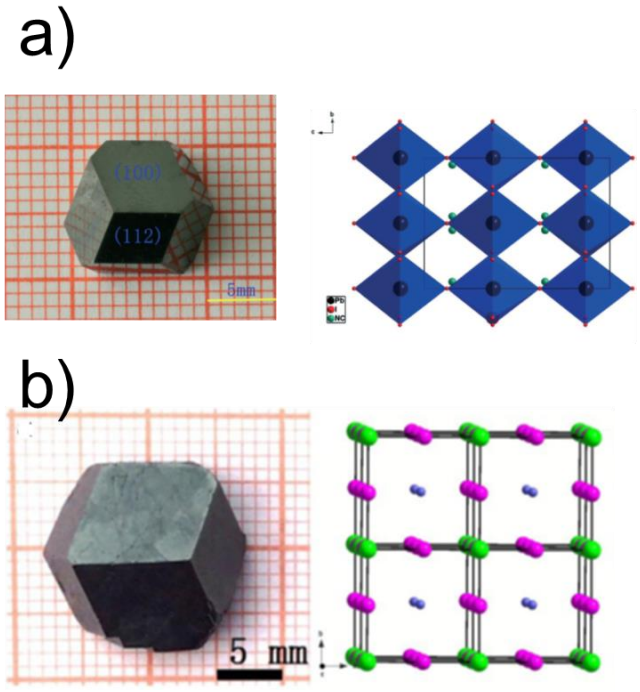

Fig. 1.3.4: *a) Tetragonal and b) cubic phases of bulk $MAPbI_3$ crystals prepared by seed solution-growth method.* Reproduced with permission.[24,39] Copyright 2015 & 2016, Royal Society of Chemistry.

1.4 Aim of this study

As described above, following the breakthrough performance of perovskites in photovoltaic device, there are various fabrication methods to synthesize nanowire (1D), thin film (2D) and bulk (3D) perovskite crystals. In particular, the fabrication of large-size single-crystal thin film (2D) perovskites is a requirement for application to optoelectronic devices. In this thesis, a simple modified solution process, namely "cast-capping" method is developed to grow thin slab-shaped and strip-shaped single-crystal perovskites with a size up to few hundreds micrometer. The principle, optimized experiment conditions and crystal structure of single-crystal $MAPbX_3$ perovskites prepared by the cast-capping method are described in chapter 2.

In chapter 3, optically pumped lasing properties of single-crystal $MAPbBr_3$ prepared by the cast-capping method are investigated. Both vertical-cavity surface-emitting lasing using a slab-shaped crystal sandwiched between distributed Bragg reflector (DBR) mirrors and Fabry-Pérot lasing between parallel side-facets of a strip-shaped crystal were achieved.

In chapter 4, electroluminescence (EL) from single-crystal $MAPbBr_3$ was investigated. Using ITO substrates in the cast-capping method, simple LEDs without any charge transport layers were fabricated. This chapter demonstrated edge-emitting and blinking EL in the single-crystal $MAPbBr_3$.

Finally, chapter 5 summarizes this thesis and give some proposal for future research following this study.

References

1. Kojima, A. *et al.* Organometal Halide Perovskites as Visible-Light Sensitizers for Photovoltaic Cells. *J. Am. Chem. Soc.* **131,** 6050–6051 (2009).
2. Kim, H. *et al.* Lead Iodide Perovskite Sensitized All-Solid-State Submicron Thin Film Mesoscopic Solar Cell with Efficiency Exceeding 9%. *Sci. Rep.* **2,** 591 (2012).
3. Nie, W. *et al.* High-efficiency solution-processed perovskite solar cells with millimeter-scale grains. *Science* **347,** 522–525 (2015).
4. Bella, F. *et al.* Improving efficiency and stability of perovskite solar cells with photocurable fluoropolymers. *Science* (2016). doi:10.1126/science.aah4046
5. Green, M. A. & Bein, T. Photovoltaics: Perovskite cells charge forward. *Nat. Mater.* **14,** 559–561 (2015).
6. Im, J. *et al.* 6.5% efficient perovskite quantum-dot-sensitized solar cell. *Nanoscale* **3,** 4088–4093 (2011).
7. Lee, M. M. *et al.* Efficient hybrid solar cells based on meso-superstructured organometal halide perovskites. *Science* **338,** 643–648 (2012).
8. Heo, J. H. *et al.* Efficient inorganic–organic hybrid heterojunction solar cells containing perovskite compound and polymeric hole conductors. *Nat. Photonics* **7,** 486–491 (2013).
9. Burschka, J. *et al.* Sequential deposition as a route to high-performance perovskite-sensitized solar cells. *Nature* **499,** 316–319 (2013).
10. Liu, M., Johnston, M. B. & Snaith, H. J. Efficient planar heterojunction perovskite solar cells by vapour deposition. *Nature* **501,** 395–398 (2013).
11. Zhou, H. *et al.* Interface engineering of highly efficient perovskite solar cells. *Science* **345,** 542–546 (2014).
12. Yang, W. S. *et al.* Iodide management in formamidinium-lead-halide-based perovskite layers for efficient solar cells. *Science* **356,** 1376–1379 (2017).
13. Yang, W. S. *et al.* High-performance photovoltaic perovskite layers fabricated through intramolecular exchange. *Science* **348,** 1234–1237 (2015).
14. Sutherland, B. R. & Sargent, E. H. Perovskite photonic sources. *Nat. Photonics* **10,** 295–302 (2016).
15. Tan, Z. *et al.* Bright light-emitting diodes based on organometal halide perovskite. *Nat. Nanotechnol.* **9,** 687–692 (2014).
16. Cho, H. *et al.* Overcoming the electroluminescence efficiency limitations of perovskite light-emitting diodes. *Science* **350,** 1222–1225 (2015).
17. Zhu, H. *et al.* Lead halide perovskite nanowire lasers with low lasing thresholds

and high quality factors. *Nat. Mater.* **14,** 636–642 (2015).

18. Kim, Y. H. *et al.* Multicolored organic/inorganic hybrid perovskite light-emitting diodes. *Adv. Mater.* **27,** 1248–1254 (2015).
19. Veldhuis, S. A. *et al.* Perovskite Materials for Light-Emitting Diodes and Lasers. *Adv. Mater.* **28,** 6804–6834 (2016).
20. Stranks, S. D. & Snaith, H. J. Metal-halide perovskites for photovoltaic and light-emitting devices. *Nat. Nanotechnol.* **10,** 391–402 (2015).
21. Stoumpos, C. C. & Kanatzidis, M. G. The Renaissance of Halide Perovskites and Their Evolution as Emerging Semiconductors. *Acc. Chem. Res.* **48,** 2791–2802 (2015).
22. Saparov, B. & Mitzi, D. B. Organic−Inorganic Perovskites: Structural Versatility for Functional Materials Design. *Chem. Rev.* **116,** 4558–4596 (2016).
23. Mitzi, D. B. *Synthesis, Structure, and Properties of Organic-Inorganic Perovskites and Related Materials*. (John Wiley & Sons, Inc., 1999).
24. Luan, M. *et al.* Controllable Growth of Bulk Cubic-Phase $CH_3NH_3PbI_3$ Single Crystal with Exciting Room-Temperature Stability. *CrystEngComm* **18,** 5257–5261 (2016).
25. Kawamura, Y., Mashiyama, H. & Hasebe, K. Structural Study on Cubic-Tetragonal Transition of $CH_3NH_3PbI_3$. *J. Phys. Soc. Japan* **71,** 1694–1697 (2002).
26. Li, G. *et al.* Efficient Light-Emitting Diodes Based on Nanocrystalline Perovskite in a Dielectric Polymer Matrix. *Nano Lett.* **15,** 2640–2644 (2015).
27. Xiao, Z. *et al.* Efficient perovskite light-emitting diodes featuring nanometre-sized crystallites. *Nat. Photonics* **11,** 108–115 (2017).
28. Xing, G. *et al.* Low-temperature solution-processed wavelength-tunable perovskites for lasing. *Nat. Mater.* **13,** 476–480 (2014).
29. Im, J., Kim, H. & Park, N. Morphology-photovoltaic property correlation in perovskite solar cells: One-step versus two-step deposition of $CH_3NH_3PbI_3$. *APL Mater.* **2,** 81510 (2014).
30. Thakur, U. *et al.* Investigation into the Advantages of Pure Perovskite Film without PbI_2 for High Performance Solar Cell. *Sci. Rep.* **6,** 35994 (2016).
31. Wu, J. *et al.* DMF as an Additive in a Two-Step Spin-Coating Method for 20% Conversion Efficiency in Perovskite Solar Cells. *ACS Appl. Mater. Interfaces* **9,** 26937–26947 (2017).
32. Lee, Y. H. *et al.* Unraveling the Reasons for Efficiency Loss in Perovskite Solar Cells. *Adv. Funct. Mater.* **25,** 3925–3933 (2015).
33. Ha, S. T. *et al.* Synthesis of Organic-Inorganic Lead Halide Perovskite

Nanoplatelets: Towards High-Performance Perovskite Solar Cells and Optoelectronic Devices. *Adv. Opt. Mater.* **2,** 838–844 (2014).

34. Zhang, Q. *et al.* Room-Temperature Near-Infrared High‐Q Perovskite Whispering-Gallery Planar Nanolasers. *Nano Lett.* **14,** 5995–6001 (2014).
35. Wong, A. B. *et al.* Growth and Anion Exchange Conversion of $CH_3NH_3PbX_3$ Nanorod Arrays for Light-Emitting Diodes. *Nano Lett.* **15,** 5519–5524 (2015).
36. Chen, Y. *et al.* Structure and Growth Control of Organic–Inorganic Halide Perovskites for Optoelectronics: From Polycrystalline Films to Single Crystals. *Adv. Sci.* (2016). doi:10.1002/advs.201500392
37. Shi, D. *et al.* Low trap-state density and long carrier diffusion in organolead trihalide perovskite single crystals. *Science* **347,** 519–522 (2015).
38. Fang, Y. *et al.* Highly narrowband perovskite single-crystal photodetectors enabled by surface-charge recombination. *Nat. Photonics* **9,** 679–686 (2015).
39. Dang, Y. *et al.* Bulk crystal growth of hybrid perovskite material $CH_3NH_3PbI_3$. *CrystEngComm* **17,** 665–670 (2015).

Chapter 2
Crystal growth by cast-capping method

The simple solution fabrication process of perovskites gives opportunities of this kind of materials for practical device applications. The performance of photovoltaic devices is improved by factor of more than ten just by optimizing fabrication processes. This chapter presents a modified solution process, namely “cast-capping” method, which affords to grow planar crystals with large single-domain sizes[1,2]. The formation of $MAPbX_3$ (X = Cl, Br or I) and their mixture ($MAPbCl_xBr_{3-x}$ and $MAPbBr_yI_{3-y}$) were investigated. Both halogen compounds, substrate surface properties and concentration of precursor solution affect dimensional growth of these perovskite crystals.

2.1 Introduction

As we know, most of the perovskite applications are based on polycrystalline thin films, which usually contain a large density of trap states at the grain boundary.[3] Single-crystal perovskites are expected that single-crystal-based devices will have much better optoelectronic performances because of no grain boundary effects. Chapter 1 already discussed about representative methods to fabricate perovskites. Beside the advantages, there are each drawback in these methods. This chapter describes the "cast-capping" method, to fabricate large-size single crystals of $CH_3NH_3PbX_3$ perovskites and their mix-halogen perovskites.[1,2,4] This method is a low-cost solution process to fabricate thin planar single-crystal perovskites which can widely applied to optoelectronic and photonic devices. By controlling the precursor concentration and substrate properties, the formation and crystal structure of all kind of methylammonium halide perovskites and their mixtures were investigated.

2.2 Experimental

2.2.1 Preparation

MAX (Wako) and PbX_2 (Alfa Aesar) were dissolved in a polar solvent such as DMF (Wako) or DMSO (Nakalai tesque). Due to faster evaporation of DMF in comparison with DMSO, the DMF was used to dissolved (MAI + PbI_2) and (MABr + $PbBr_2$). In the case of (MACl + $PbCl_2$), both DMF and DMSO solvents were used to investigate the influence of solvents on the crystal formation of the $MAPbCl_3$. In principle, single-crystal perovskites are formed according to the following reaction:

$$CH_3NH_3X + PbX_2 \rightleftharpoons CH_3NH_3PbX_3 \qquad (1)$$

Moreover, the crystal formation depends on substrate surface properties, MAX:PbX_2 ratio in the precursor solution. The details are described in the next section below. Glass slides, mica, distributed Bragg reflector (DBR) and ITO-coated glass were used as substrates for single-crystal growth by the cast-capping method. These substrates were washed in acetone, methanol and 2-propanol for 15 minutes in an ultrasonic bath then dried in an air oven at 80°C for 2 minutes before treated in UV-ozone exposure for 10 minutes.

The cast-capping method consists of two simple steps: casting the precursor solution

on a substrate surface, then capping with another substrate as shown in Fig. 2.2.1. The sample was left to naturally dry at room temperature in ambient condition for few days.

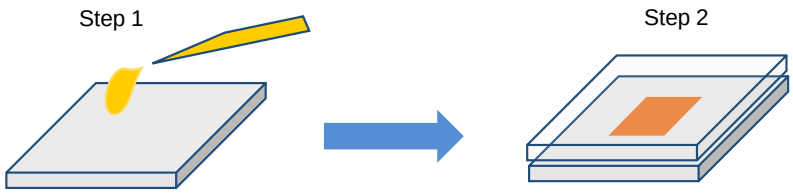

Fig. 2.2.1: *Schematic of cast-capping method. The perovskite solution is casted on a substrate (step 1), then capped with another substrate (step 2).*

As schematically shown in Fig. 2.2.2, during the drying process the concentration of precursor solution increases and forms crystal nuclei following the reaction (1). Due to slow evaporation of used solvents, the lateral growth proceeds keeping the tension between the top and bottom substrates. The crystal expansion is completed in the cavity between two substrates until the solvent is fully evaporated.

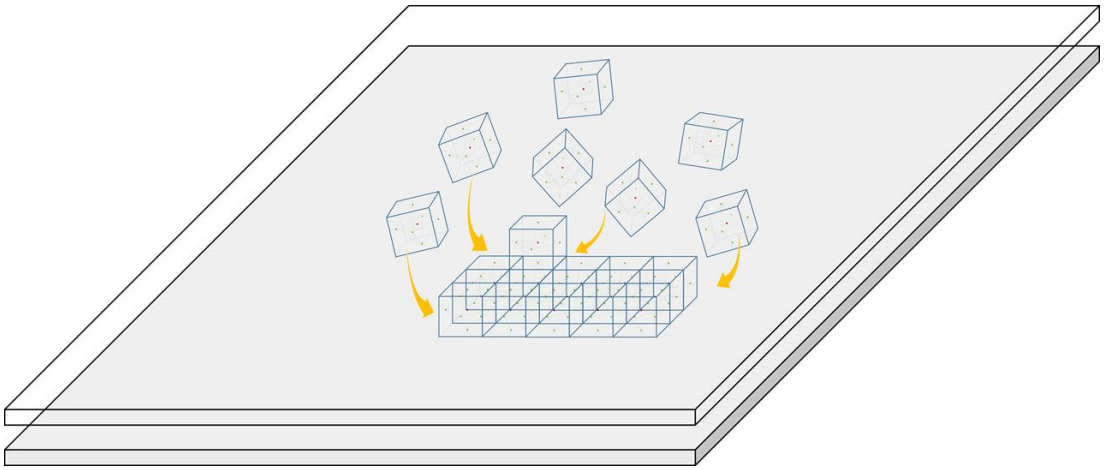

Fig. 2.2.2: *Schematic of crystal growth in the cavity between the substrates.*

2.2.2 Characterization

A transmission optical microscope (Olympus BX-51) was used to study crystal morphology of the fabricated perovskites. Their crystallinity was observed under crossed nicols polarization by rotating the sample. The crystal formation and orientation were examined by X-ray diffraction (XRD) using a X-ray diffractometer (Rigaku RINT-TT III/NM). To carry out the XRD measurements, the substrate/perovskite/substrate samples were cleaved and the crystal left on either substrate was measured by θ/2θ scan. For reference as an isotropic sample, the crystals on the substrate was scratched off into fine powders.

2.3 Crystal formation

2.3.1 $MAPbBr_3$ crystals

To prepare single-crystal $MAPbBr_3$ by the cast-capping method, glass, mica and ITO were used as substrate with a stoichiometric molar ratio of $MABr:PbBr_2$ (= 1:1). Fig. 2.3.1 shows optical micrographs of representative samples denoted as capping substrate (top)/$MAPbBr_3$/casting substrate (bottom). In all these samples, two-dimensionally spreading planar single crystals grow between the top and bottom substrates. The well-shaped right-angled corners indicate that the dimension of single-crystal domains is approaching up to a millimeter scale. The large rectangle-shaped crystal in all samples indicates that the cubic form of $MAPbBr_3$ was grown. It suggests that all substrate materials can be used to grow planar perovskite crystals in the cast-capping method.

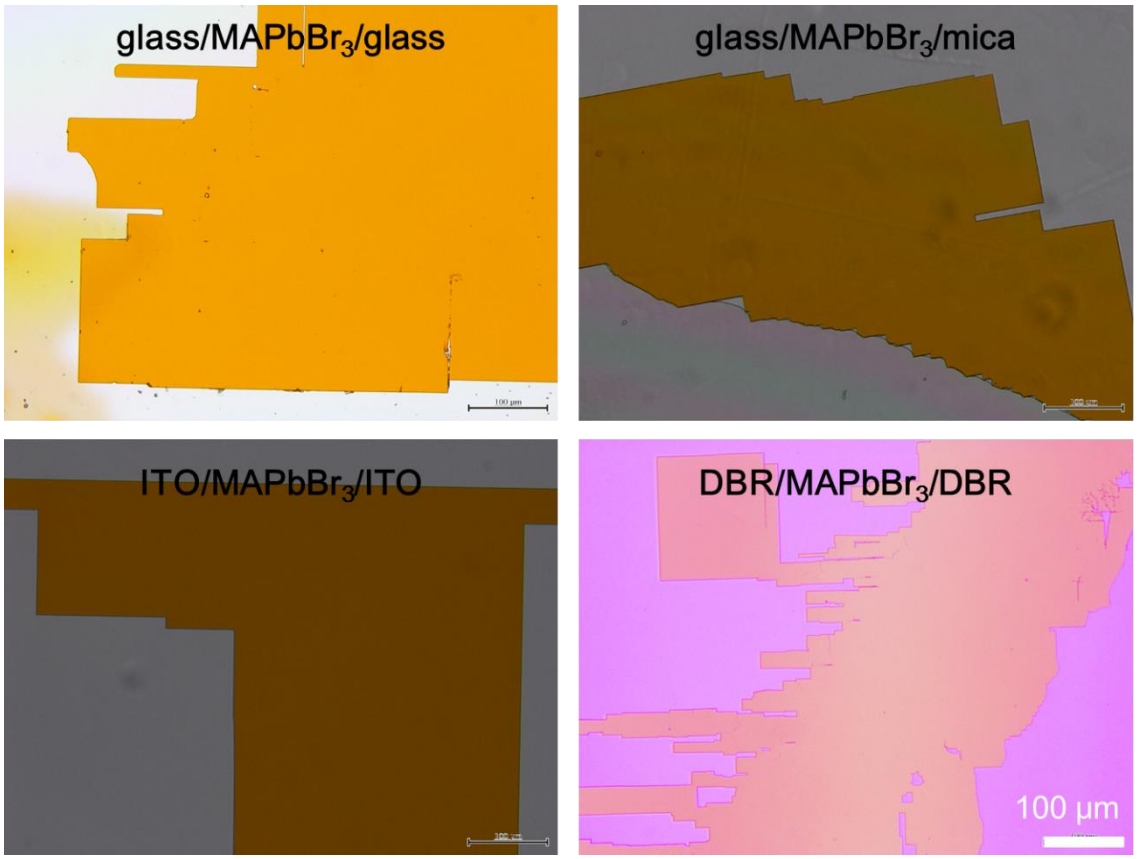

Fig. 2.3.1: *Transmission optical micrographs of $MAPbBr_3$ crystals grown in samples of glass/$MAPbBr_3$/glass, glass/$MAPbBr_3$/mica, ITO/$MAPbBr_3$/ITO and DBR/$MAPbBr_3$/DBR.*

The single crystallinity of this sample was confirmed by polarized transmission microscopy as shown in Fig. 2.3.2. The micrograph taken under the diagonal position of the crossed nicols (right) shows a homogeneous transmission over the whole crystal. When the sample was rotated by 45° to the extinction position of the nicols (left), the transmission was homogeneously vanishes, indicating that the sample is entirely a single crystal.

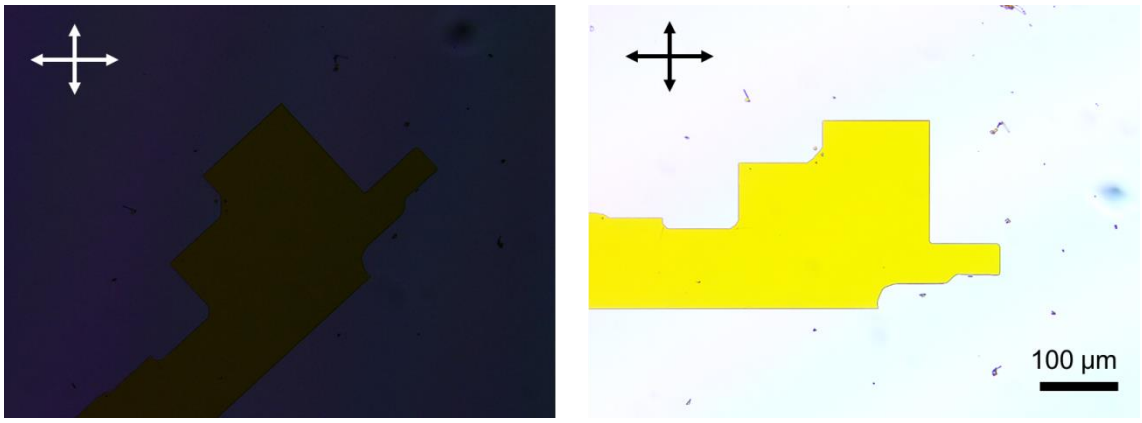

Fig. 2.3.2: *Polarized optical micrographs of $MAPbBr_3$ crystal grown between glass/glass substrates. The horizontal and vertical arrows in the images indicate the polarizer and analyzer directions of the crossed nicols, respectively.*

The structures of the $MAPbBr_3$ prepared between glass/glass and ITO/ITO substrates were examined by X-ray diffraction (XRD) shown in Fig. 2.3.3. The red-dotted and green-dash lines show $2\theta/\theta$ patterns taken from the single-crystal $MAPbBr_3$ grown between ITO/ITO and glass/glass substrates, respectively, after cleaving the sandwiched cast-capping samples. The black-solid lines show $2\theta/\theta$ patterns taken from the respective powder samples prepared by scratching off the crystals from the substrate. By using Bragg's law to convert the peak position to interplanar spacing, the peaks appearing at 14.95°, 21.15°, 30.15°, 33.75°, 37.15°, 43,10°, and 45.95° can be assigned to (100), (110), (200), (210), (211), (220), and (300) planes, respectively. The peaks of the powder $MAPbBr_3$ sample is indexed by its cubic structure with a *Pm3m* unit cell with the lattice parameter a = 5.93 Å, in accordance with the previous reports.[1,5,6] In the case of

glass/glass substrates, there are two intense peaks of (110) and (220) planes indicating that the *c*-axis of the $MAPbBr_3$ crystal orients normal to the glass surface. Noteworthy, other weak peaks at 14.95° and 30.15° correspond to the scratched crystals left when the glass/glass sample was cleaved. As a result, the (110) face of the single crystals grows planar parallel to the surface of glass. In contrast, the XRD pattern of the single-crystal $MAPbBr_3$ in the ITO/ITO samples shows 4 intense peaks of (100), (200), (300) and (400). This growing planes are different from those (110) and (220) planes in the glass/glass sample. It is concluded that the stabilization of growing faces depends on the substrate surface properties. It may suggest an energetic preference to grow [110] orientation as an initial seeds on glass.[7]

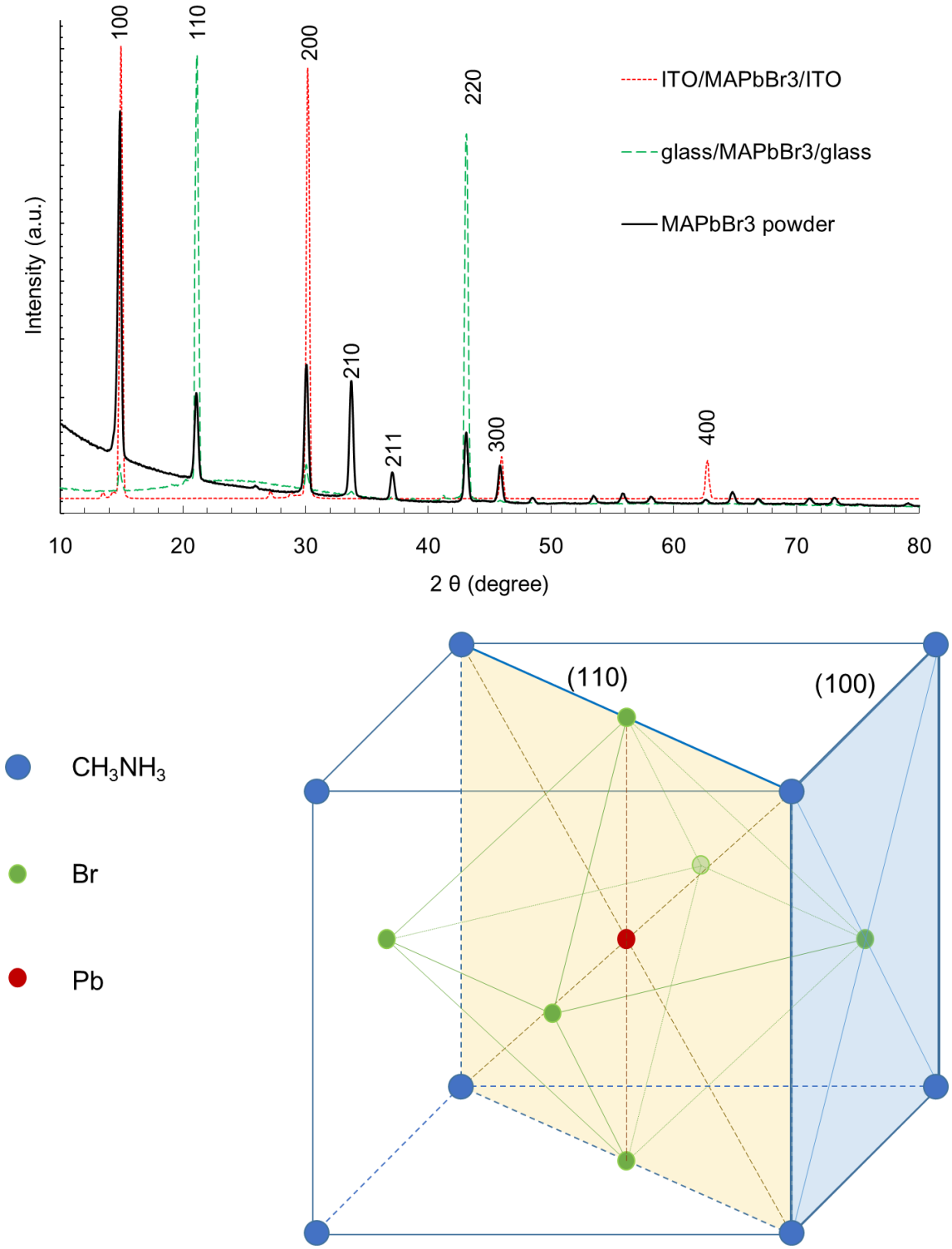

Fig. 2.3.3: *XRD patterns of single-crystal $MAPbBr_3$ grown between glass/glass and ITO/ITO substrates in comparison with reference powder sample. The bottom schematic illustrates the cubic perovskite crystal showing (100) and (110) planes.*

2.3.2 $MAPbCl_3$ crystals

The limited solubility of $MACl:PbCl_2$ in DMF resulted in the precipitation from the DMF precursor solution into small rectangle-shaped crystals with a size range of 20 – 100 μm as shown in Fig. 2.3.4. However, $MACl:PbCl_2$ is well dissolved in DMSO and the precursor concentration is able to be increased up to 10 wt%. Therefore, the crystal growth from the DMSO solution was promoted to yield large-sized single domains over several hundreds of μm.

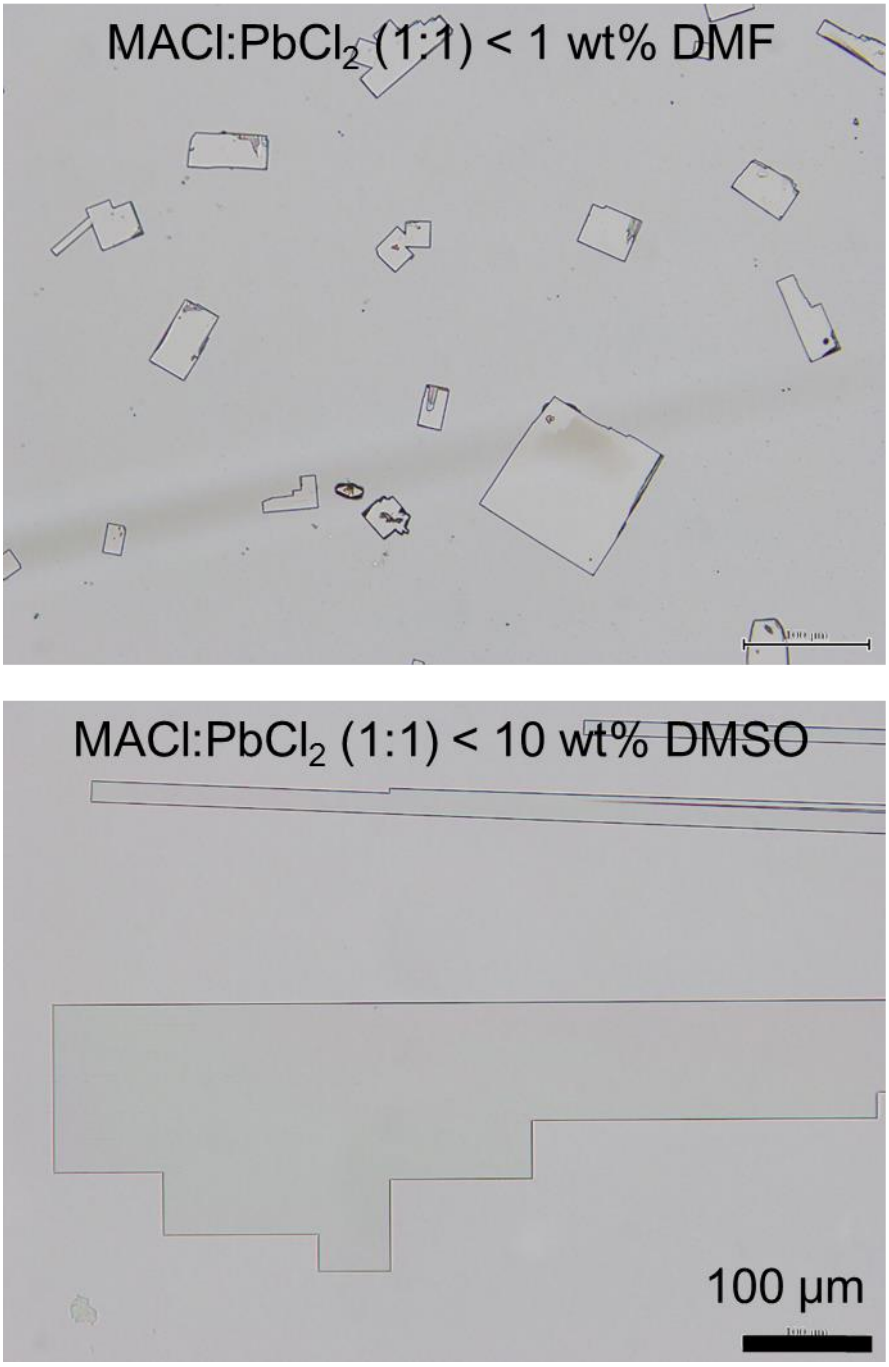

Fig. 2.3.4: *Transmission optical micrographs of $MAPbCl_3$ when crystallized from precursor solutions of DMF (top) and DMSO (bottom) between glass/glass substrate (please check).*

Structure of the $MAPbCl_3$ crystals prepared between the glass/glass substrates with MACl:$PbCl_2$ in DMSO solution was examined by XRD with $2\theta/\theta$ scan. As shown in Fig. 2.3.5, the XRD pattern of the powder $CH_3NH_3PbCl_3$ sample is indexed by its cubic structure with a *Pm3m* space group and a lattice constant a = 5.67 Å.[8,9] However, the intense peaks at 15.7° and 31.5°, which corresponds to the (100) and (200) planes of the cubic form, respectively, indicates that these planes grow planar in contact with the substrate surface. This crystal orientation is different from that of $CH_3NH_3PbBr_3$ prepared by the cast-capping method in which the (110) plane grows on the glass surface[1] while it is same as the (100) plane growth on the ITO surface. It suggests that not only surface properties but also the halogen anions affect the stabilization of those growth planes.

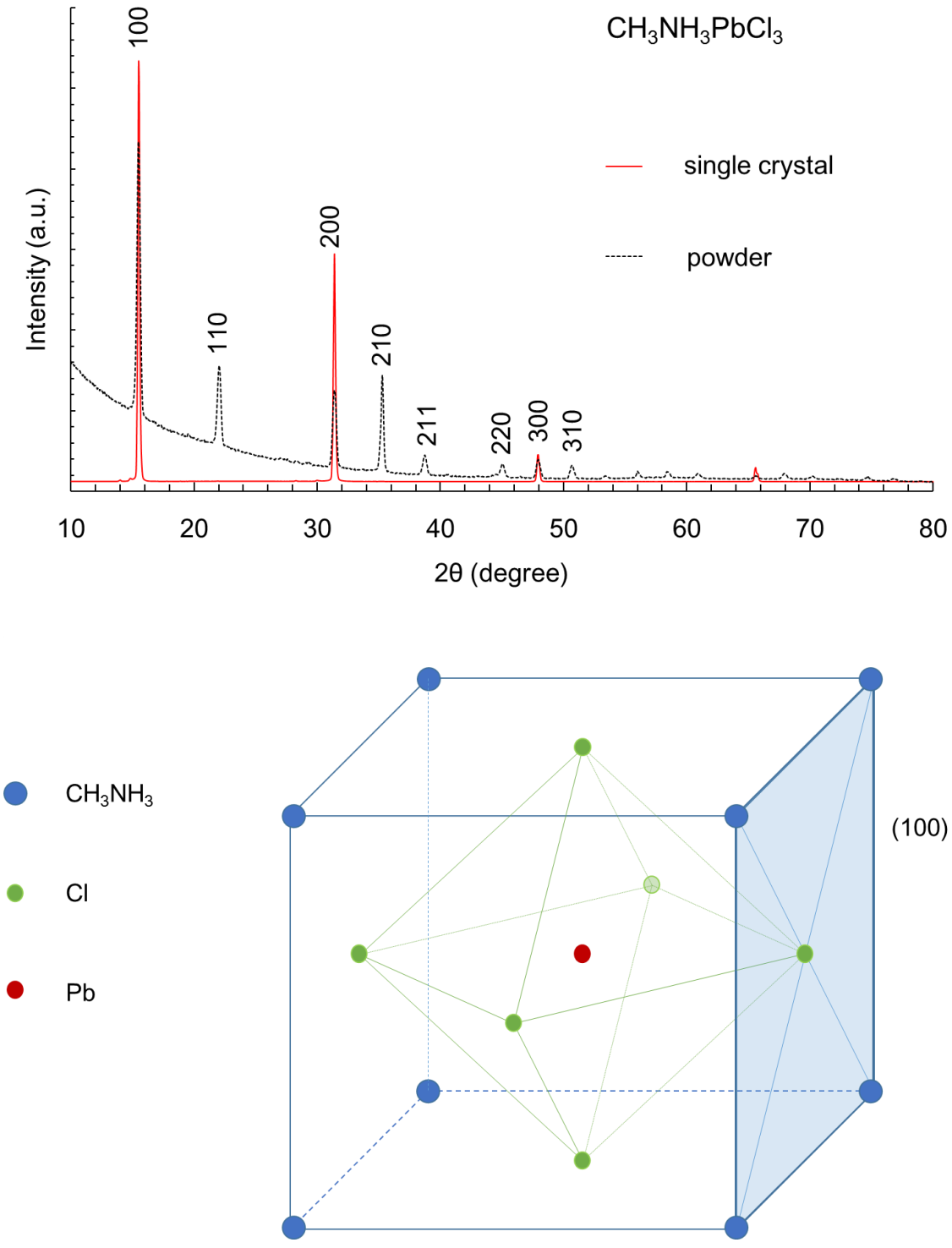

Fig. 2.3.5: *XRD patterns of single-crystal $MAPbCl_3$ in comparison with powder reference sample. The bottom schematic shows the cubic perovskite structure of $MAPbCl_3$.*

2.3.3 $MAPbI_3$ crystals

In the case of $CH_3NH_3PbI_3$ perovskite, the CH_3NH_3I:PbI_2 precursor was well dissolved in DMF, however, the stoichiometric solution of CH_3NH_3I:PbI_2 (1:1) resulted in a mixture of yellow crystals corresponding to $CH_3NH_3PbI_3$ and transparent strip-shaped precipitates (Fig. 2.3.6). The latter precipitates is assigned to unreacted PbI_2 since the cast-capping of a pure PbI_2 solution yielded a similar product. In order to improve the crystal growth of $CH_3NH_3PbI_3$, the ratio of CH_3NH_3I:PbI_2 was varied from 2:1 to 4:1. By adding an excess of CH_3NH_3I in the precursor solution, the reverse reaction producing PbI_2 is suppressed, consequently, a large-size planar domain grew in size up to few millimeters. The increased concentration of CH_3NH_3I:PbI_2 also affected the crystal growth of $CH_3NH_3PbI_3$ as shown in Fig. 2.3.7. At low concentration of 5 wt%, single crystals were formed. At concentration of 10 wt%, single-crystal $MAPbI_3$ grow larger and more homogenously. However, the crystal size is reduced at higher concentration above 20 wt%. At 30 wt%, $CH_3NH_3PbI_3$ grows in a fiber form suggesting that the high content of PbI_2 probably prohibits the single-domain growth even at the CH_3NH_3I:PbI_2 ratio of 4:1.

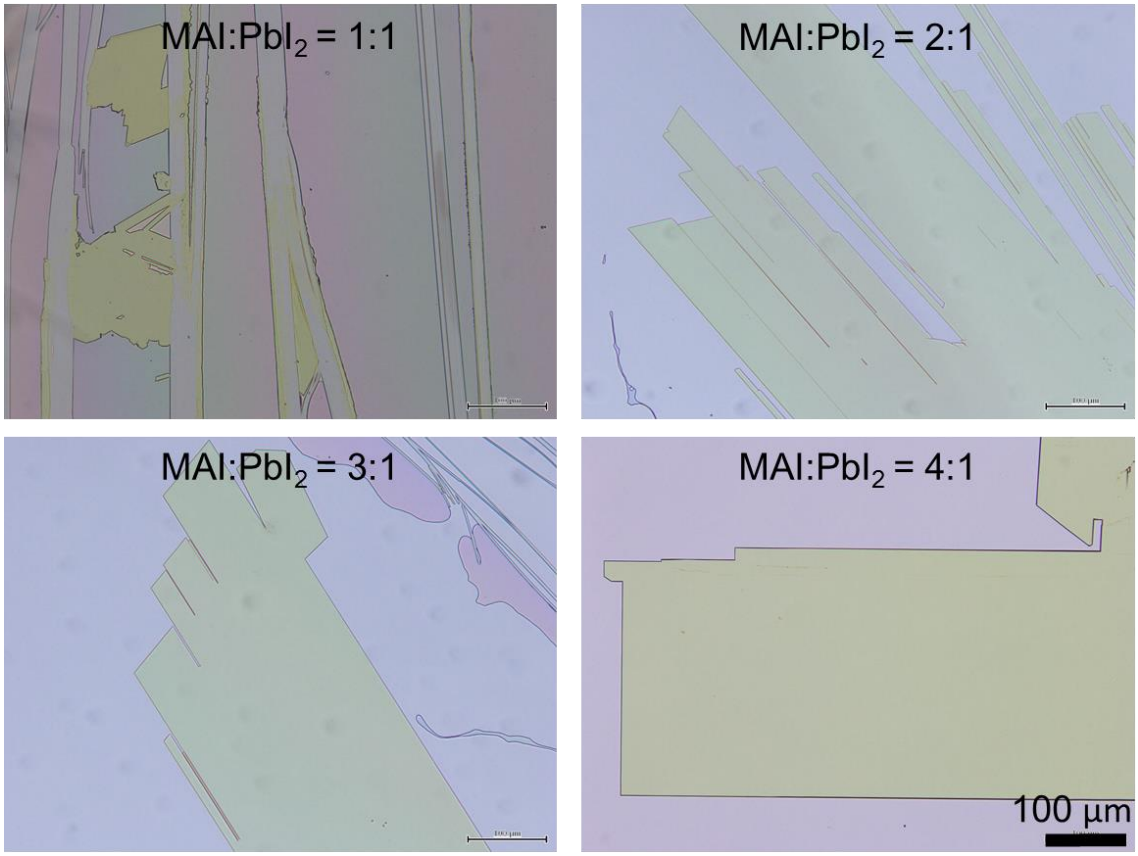

Fig. 2.3.6: *Transmission optical micrographs of $MAPbI_3$ grown between glass/glass substrates with the precursor $MAI:PbI_3$ dissolved in DMF at concentration of 10 wt%.*

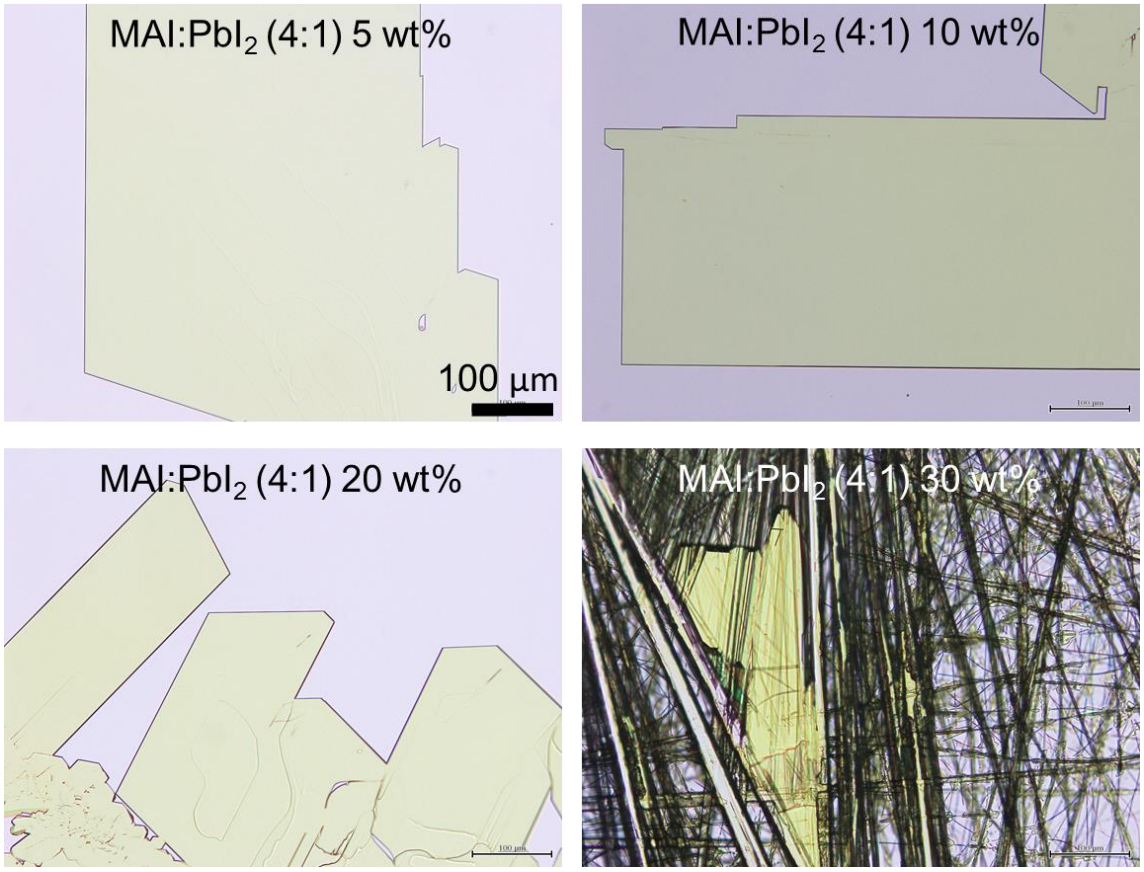

Fig. 2.3.7: *Transmission optical micrographs of $MAPbI_3$ grown between glass/glass substrates from the precursor MAI:PbI_3 (4:1) dissolved in DMF at concentration of 5, 10, 20 and 30 wt%.*

In comparison with other studies of platelets fabricated by vapor deposition[10, 11] and bulk crystals prepared by inverse temperature crystallization,[9] it is remarkable that each planar crystals obtained at the above condition consist of a single-crystalline domain. Their single crystallinity was confirmed by polarized transmission microscopy presented for $CH_3NH_3PbI_3$ in Fig. 2.3.8. The micrograph under the diagonal position of the crossed nicols shows a homogeneous transmission over the larger crystal domain (left). When the sample was rotated by 45° to the extinction position, its transmission was completely

vanished while the smaller crystal domain recovered a transmission (right) indicating that both domains are single crystals.

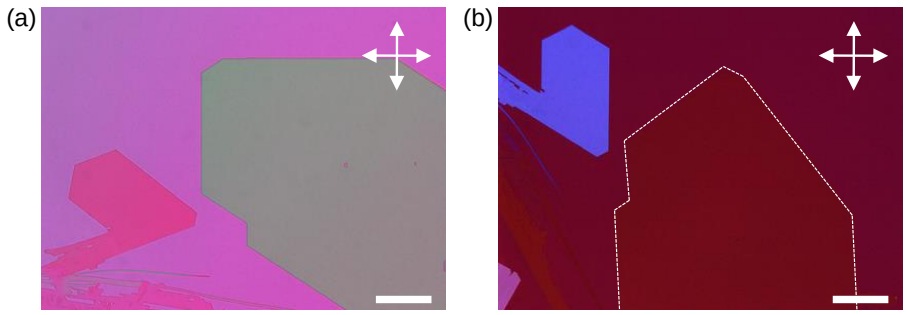

Fig. 2.3.8: *Polarized transmission optical micrographs of $CH_3NH_3PbI_3$ crystals. The horizontal and vertical arrows indicate the polarizer and analyzer directions of the crossed nicols, respectively. The sample in (b) is rotated by 45° with respect to (a). The scale bar: 100 μm.*[2]

Structures of the $CH_3NH_3PbI_3$ crystals prepared at optimized condition of $MAI:PbI_2$ ratio of 4:1 were examined by XRD as shown in Fig. 2.3.9. Similar to the previous experiments of $MAPbBr_3$ and $MAPbCl_3$, the XRD pattern of the $CH_3NH_3PbI_3$ samples is also interpreted by the cubic Pm3m unit cell with a lattice parameter a = 6.39 Å [8,12,13]. In the case of the planar crystal grown at the $CH_3NH_3I:PbI_2$ ratio of 4:1 in 10 wt% DMF (see Fig. 2.3.7), the highest diffraction peak appearing at 27.9° (red line) corresponds to the (200) plane. On the other hand, the highest peak at 19.6° (blue line) in the case of the fiber crystals grown at the $CH_3NH_3I:PbI_2$ ratio of 4:1 in 30 wt% DMF (see Fig. 2.3.7)

corresponds to the (110) plane of the cubic form. It suggests that not only the crystal morphology but also the growth plane of the cubic crystals in contact with substrate surface is also sensitive to the precursor concentration.

These observations are in remarkable contrast to other fabrication methods at room temperature resulting in tetragonal structure of $CH_3NH_3PbI_3$ [11,14,15]. The previous studies have reported that the cubic $CH_3NH_3PbI_3$ is changed to tetragonal structure at temperature lower than 60°C.[8] Contrastingly, in 2015, L. Wang et al. found stable cubic $MAPbI_3$ crystals at room temperature by the aid of chlorine and TiO_2 layer for reducing the cubic to tetragonal transition temperature. Recently, a bulk cubic crystal was also formed at room temperature by combining anti-solvent and temperature conditions.[12] In the present study, the slow growth rate in the cast-capping method which avoids an exposure of the sample to the ambient air probably promotes the growth of cubic phases. Note that, however, the XRD pattern of the $CH_3NH_3PbI_3$ sample shows unknown peaks which are not assigned to the tetragonal form nor to unreacted CH_3NH_3I and PbI_2. It might arise from decomposed species since the sample color gradually changes from yellow to black after cleaving the cast-capping substrates for the XRD measurement in air.

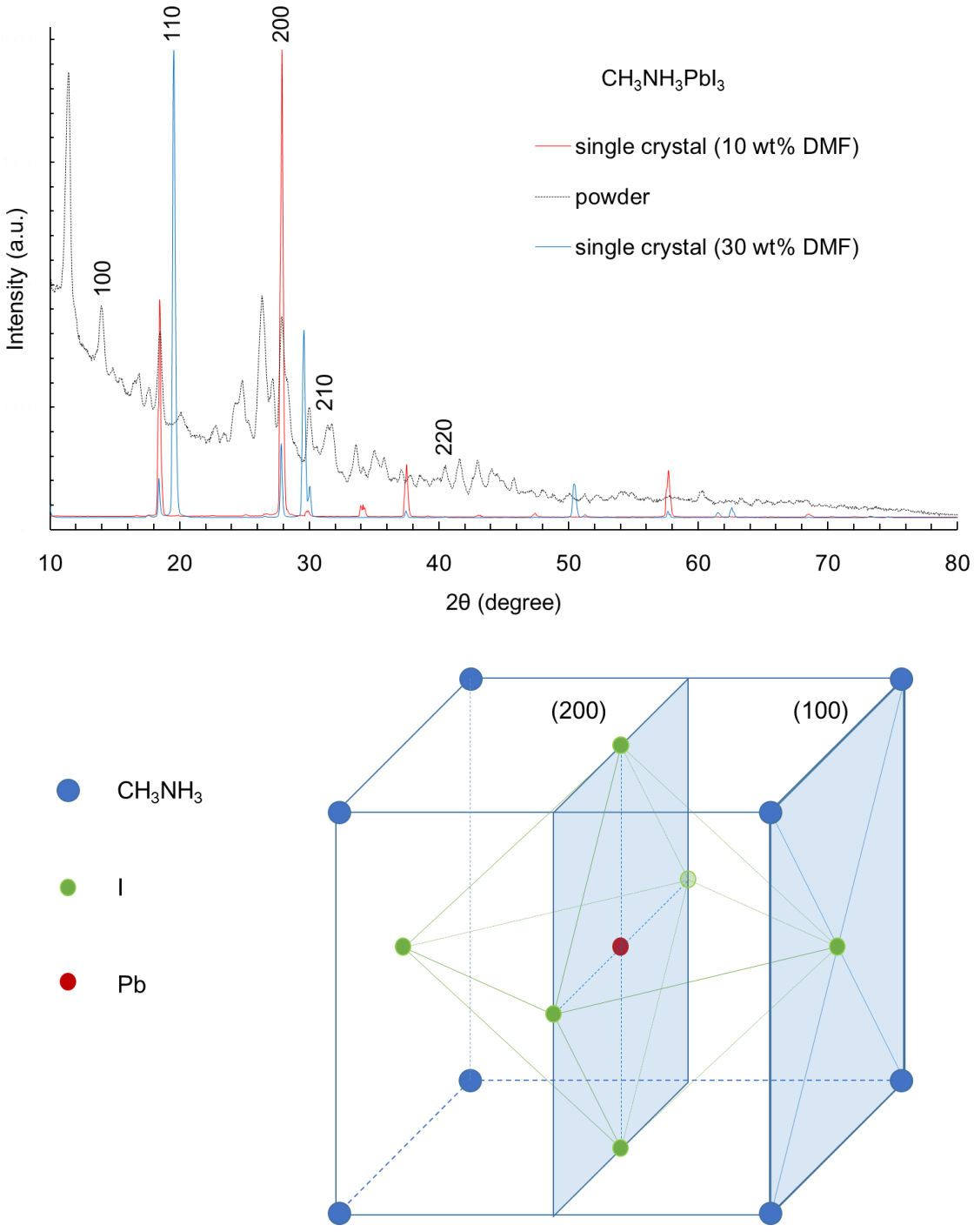

Fig. 2.3.9: *XRD patterns of single-crystal $MAPbI_3$ in comparison with powder reference sample. The bottom schematic shows the cubic crystal structure of $MAPbI_3$.*

2.3.4 Mixture Perovskites

A major advantage of lead halide perovskites is their broad wavelength tunability based on controllable stoichiometry. By using either mixtures of bromides and iodides or chlorides and iodides, the emission is continuously tunable over the entire visible spectral range (from ~390 to 790 nm) suggesting their bandgaps depend on the Br/I or Cl/Br ratio in the perovskite crystals.[16] Surprisingly, X-Y. Zhu et al. successfully fabricated single-crystal perovskite nanowires with various stoichiometry and indicated exceptional lasing performance with color tunability from near-infrared to blue.[17] In this section, the cast-capping method was applied to grow single-crystal mixture perovskites.

In principle, the mixture perovskites are formed by the following reactions:

$$MA^+ + Pb^{2+} + xBr^- + (3-x)I^- \rightleftharpoons MAPbBr_xI_{3-x} \quad (2)$$

$$MA^+ + Pb^{2+} + yBr^- + (3-y)Cl^- \rightleftharpoons MAPbBr_yCl_{3-y} \quad (3)$$

By simply mixing different amounts of MAI:MABr or MABr:MACl with $PbBr_2$, single-crystal perovskites with different mixture ratios can be grown in the cavity between the tops/bottom substrates as shown in Fig. 2.3.10. Their luminescence changes from blue for $MAPbBr_{2.5}Cl_{0.5}$ to red for $MAPbBr_{2.5}I_{0.5}$ in comparison with the green color of the $MAPbBr_3$ crystal.

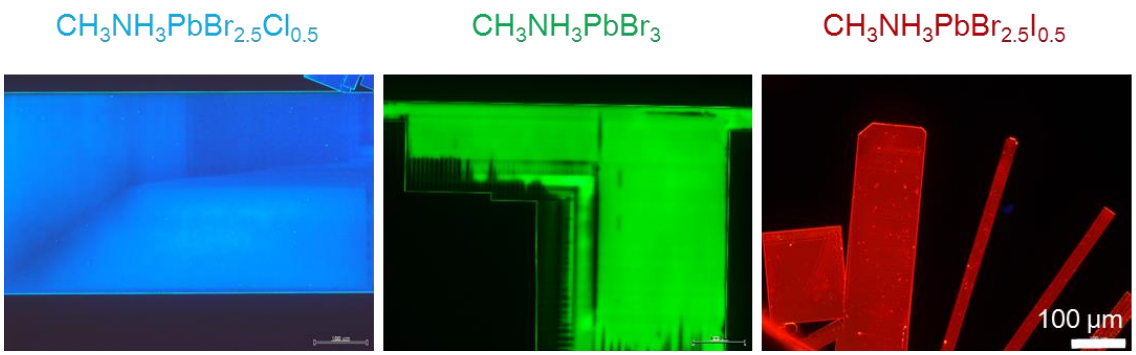

Fig. 2.3.10: *Photoluminescence micrographs of mixture single-crystal perovskites.*

To identify the halide compositions in the single crystals, XRD measurements were carried out and the crystal structure of these mixture single-crystal perovskites were analyzed. All substrates here used to prepare single-crystal mixture perovskites are glass. Their XRD patterns are shown in Fig. 2.3.11. In the case of $MAPbBr_yCl_{3-y}$, the diffraction peaks shift to the higher angle with increasing Cl^- precursor ratio, indicating decreased lattice constants due to the smaller ionic radius of Cl^-. The growth planes of the mixture perovskite crystals are also identified from their XRD patterns.

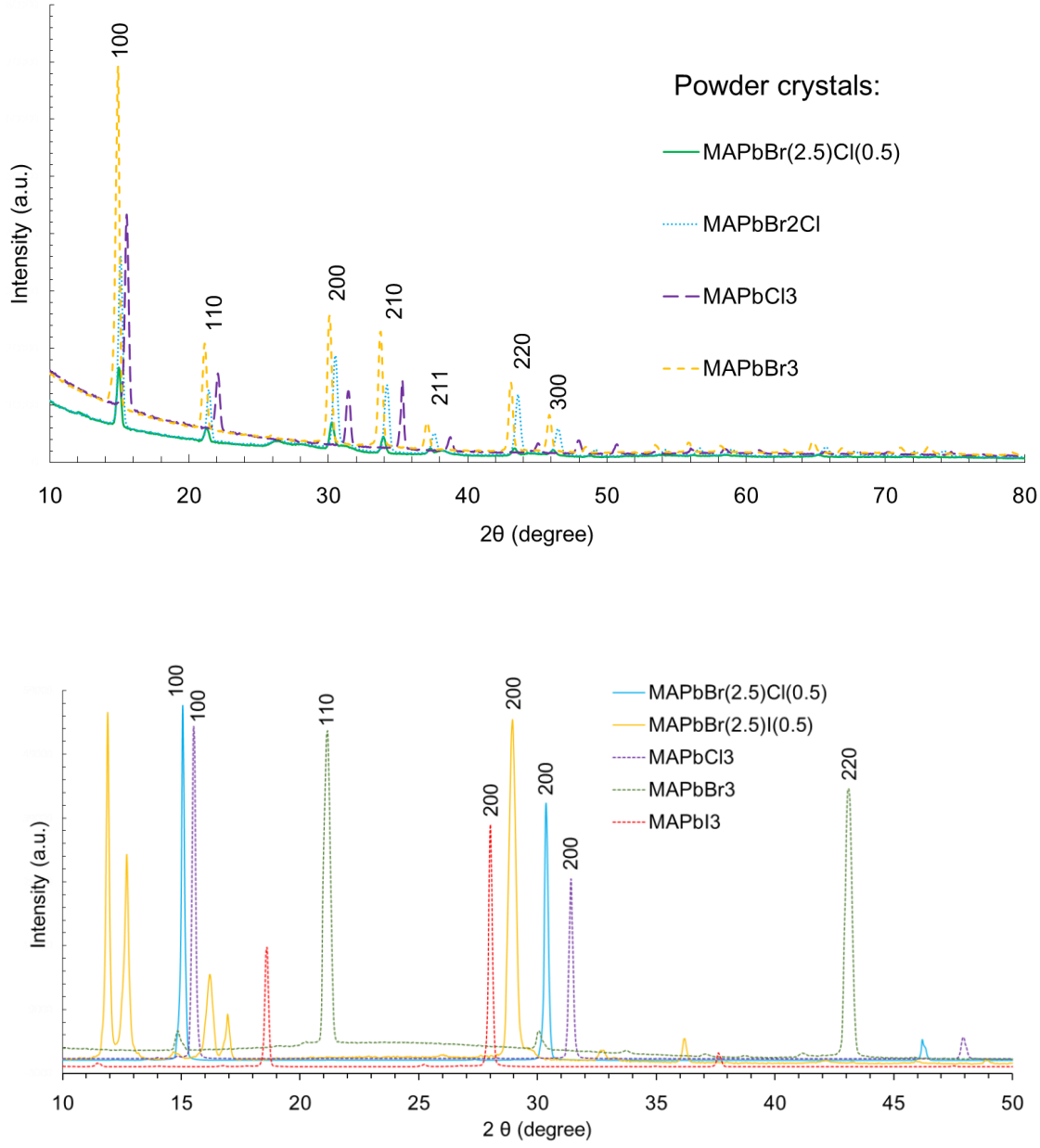

Fig. 2.3.11: *XRD patterns of mixture single-crystal $MAPbBr_xI_{3-x}$ and $MAPbBr_yCl_{3-y}$ in comparison with single-crystal $MAPbX_3$ (X=Cl, Br, I).*

All XRD patterns showed a good match with their cubic crystal structures. Noteworthy, the addition of iodide and chlorine anions changed the growth plane of (110) for $MAPbBr_3$ to (100) plane in parallel to the glass substrates. Using Bragg's law to calculate the lattice constant of these single-crystal perovskites, the lattice constants of these crystals are summarized in Table 2. The smallest atomic radius of chlorine resulted in the smallest lattice constant of 5.67 Å for $MAPbCl_3$. With increasing larger inions of Br^-.and I^- in the single-crystal perovskite, the lattice constant is increased gradually up to 6.39 Å for $MAPbI_3$.

Table 2: *Dependence of lattices constants of cubic single-crystal perovskites on halogen composition.*

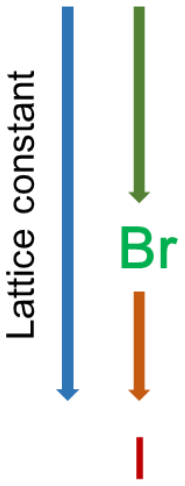

	d (Å)
$CH_3NH_3PbCl_3$	5.67
$CH_3NH_3PbBr_2Cl$	5.86
$CH_3NH_3PbBr_{2.5}Cl_{0.5}$	5.91
$CH_3NH_3PbBr_3$	5.93
$CH_3NH_3PbBr_{2.5}I_{0.5}$	6.16
$CH_3NH_3PbI_3$	6.39

2.4 Summary

In summary, the simple solution process, cast-capping method was successfully adopted to prepare thin planar single crystals for all kinds of methylammonium lead halide perovskites between various substrates. All crystals obtained belonged to the cubic structure with *Pm3m* space group. The lattice constants of these single crystals were dependent on the halide compositions as shown in Table 3. This simple cast-capping method provides remarkable usefulness to prepare two-dimensionally grown thin planar single-crystal perovskites which are in particular demanded for fabrication of not only photovoltaic but also light-emitting and other optoelectronic device.

Table 3: *The single-crystal perovskites grown by cast-capping method.*

Substrates / $MAPbX_3$	Growth planes		Lattice Constant (Å)
	Glass/glass	ITO/ITO	
Cl	100	-	5.67
$ClBr_2$	100	-	5.86
$Cl_{0.5}Br_{2.5}$	100	-	5.91
Br	110	100	5.93
$Br_{2.5}I_{0.5}$	100	-	6.16
I	100	-	6.39

References

1. Nguyen, V. C. *et al.* Optically pumped lasing in simple solution-processed single crystals of organometal halide perovskites. *Appl. Phys. Lett.* **108,** 261105 (2016).
2. Nguyen, V. C. *et al.* Single-crystal perovskites prepared by simple solution process : Cast- capping method. *J. Cryst. Growth* **468,** 796–799 (2017).
3. DeQuilettes, D. W. *et al.* Impact of microstructure on local carrier lifetime in perovskite solar cells. *Science* **348,** 683–686 (2015).
4. Sasaki, F. *et al.* Optically pumped lasing in solution-processed perovskite semiconducting materials: Self-assembled Fabry–Pérot microcavity. *Jpn. J. Appl. Phys.* **56,** 04CL07 (2017).
5. Shi, D. *et al.* Low trap-state density and long carrier diffusion in organolead trihalide perovskite single crystals. *Science* **347,** 519–522 (2015).
6. Saidaminov, M. I. *et al.* High-quality bulk hybrid perovskite single crystals within minutes by inverse temperature crystallization. *Nat. Commun.* **6,** 7586 (2015).
7. Koza, J. A. *et al.* Epitaxial Electrodeposition of Methylammonium Lead Iodide Perovskites. *Chem. Mater.* **28,** 399-405 (2015).
8. Oku, T. Crystal Structures of CH3NH3PbI3 and Related Perovskite Compounds Used for Solar Cells. *Sol. Cells - New Approaches Rev.* 77–101 (2015). doi:10.5772/58490
9. Maculan, G. *et al.* CH3NH3PbCl3 Single Crystals: Inverse Temperature Crystallization and Visible-Blind UV-Photodetector. *J. Phys. Chem. Lett.* **6,** 3781–3786 (2015).
10. Zhang, Q. *et al.* Room-Temperature Near-Infrared High‐Q Perovskite Whispering-Gallery Planar Nanolasers. *Nano Lett.* **14,** 5995–6001 (2014).
11. Ha, S. T. *et al.* Synthesis of Organic-Inorganic Lead Halide Perovskite Nanoplatelets: Towards High-Performance Perovskite Solar Cells and Optoelectronic Devices. *Adv. Opt. Mater.* **2,** 838–844 (2014).
12. Luan, M. *et al.* Controllable Growth of Bulk Cubic-Phase $CH_3NH_3PbI_3$ Single Crystal with Exciting Room-Temperature Stability. *CrystEngComm* **18,** 5257–5261 (2016).
13. Wang, Q. *et al.* Transition from the Tetragonal to Cubic Phase of Organohalide Perovskite: The Role of Chlorine in Crystal Formation of $CH_3NH_3PbI_3$ on TiO2 Substrates. *J. Phys. Chem. Lett.* **6,** 4379–4384 (2015).
14. Dong, Q. *et al.* Electron-hole diffusion lengths > 175 um in solution-grown $CH_3NH_3PbI_3$ single crystals. *Science* **347,** 967–970 (2015).

15. Chiang, C. H., Tseng, Z. L. & Wu, C. G. Planar heterojunction perovskite/$PC_{71}BM$ solar cells with enhanced open-circuit voltage via a (2/1)-step spin-coating process. *J. Mater. Chem. A* **2,** 15897–15903 (2014).
16. Xing, G. *et al.* Low-temperature solution-processed wavelength-tunable perovskites for lasing. *Nat. Mater.* **13,** 476–480 (2014).
17. Zhu, H. *et al.* Lead halide perovskite nanowire lasers with low lasing thresholds and high quality factors. *Nat. Mater.* **14,** 636–642 (2015).

Chapter 3
Optically pumped lasing from single-crystal $MAPbBr_3$ prepared by cast-capping method

In the previous chapter, all kinds of single-crystal methylammonium halide perovskites were successfully grown in the planar cavity between various substrate materials by the cast-capping method. In this chapter, their optically pumped lasing properties were investigated for representative single-crystal cavities of $MAPbBr_3$. The edge-emitting lasing was observed based on Fabry-Pérot resonation between parallel side facets of a strip-shaped crystal typically with a lateral cavity length of a few tens of μm. In order to introduce an external-optical resonance, a vertical-cavity surface-emitting laser (VCSEL) was fabricated by using DBR mirrors for the top/bottom substrates in the cast-capping method. As a result, simultaneous detection of the edge- and surface-emitting lasing was observed from the strip-shaped and slab-shaped regions of the single-crystal $MAPbBr_3$, respectively. It revealed that the thickness gradient in the slab-shaped crystal led to a higher threshold excitation fluence in the VCSEL as compared to the edge-emitting laser based on the Fabry-Pérot resonation by the strip-shaped crystal facets[1].

3.1 Introduction

Besides superior light-absorption properties in photovoltaic cells, solid-state perovskites have shown great advantages also as light-emitting sources.[2–6] The family of methylammonium lead halide perovskites, is a hybrid inorganic-organic direct-bandgap light emitter, spectrally tunable through halide stoichiometry.[7] Their low-cost solution-process fabrication is also highly compatible with printing technologies[8] and integrative with silicon-based technologies[9]. By using simple solution-processed spin-coating method to prepare crystalline perovskites thin films, T. C. Sum et al. observed amplified spontaneous emitting (ASE) at a low excitation threshold of 12 $\mu J/cm^2$ and high absorption coefficient up to 5.7×10^4 cm^{-1} for $MAPbI_3$.[10] In addition, the continuously tunable ASE wavelengths in a wide range of 390 ~ 790 nm was realized by mixing halogens (X = Cl, Br, I) at various ratios in the precursor solution of MAX and PbX_2. Another study by Q. Xiong et al. investigated lasing in nanoplatelets of $MAPbI_3$ prepared by vapor deposition on mica substrate.[11] The whispering-gallery mode (WGM) lasing was observed from a triangle nanoplatelet with a cavity-quality factor (Q) factor of ~ 650 at an excitation threshold of 37 $\mu J/cm^2$. Moreover, very low lasing threshold of 220 nJ/cm^2, high Q factor of 3,600 and nearly unit photoluminescence quantum yield (PLQY) were achieved for nanowire perovskites at room temperature.[12] This low lasing threshold for

the nanowire perovskite corresponds to a charge carrier density of 1.5×10^{16} cm^{-3} which is two-order magnitude smaller than that (1.7×10^{18} cm^{-3}) of crystalline thin films.[10,12]

It suggests that the lasing performance of perovskites as optical gain media is remarkably governed by the crystal-cavity quality which depends on the fabrication techniques. In this study, the single-crystal perovskites with well-shaped low-dimensional morphology prepared by the cast-capping method are promising as high-performance lasing media. In this chapter, optically pumped lasing properties were investigated for representative single-crystal cavities of $MAPbBr_3$.

3.2 Experimental

Following the fabrication process described in chapter 2, single-crystal $MAPbBr_3$ cavities were fabricated by the cast-capping method using glass/glass (Fig. 3.2.1a) and DBR/DBR (Fig.3.2.1b) substrates. After fully dried, the samples were provided for the optical measurements. An excitation source of a Ti:sapphire optical amplifier ($\lambda = 397$ nm, 200 fs duration, and 1 kHz repetition) was used for optical pumping the single-crystal $MAPbBr_3$ cavities. The p-polarized excitation beam was focused to a spot size of ~ 25 × 60 μm^2 through the top substrate at an incident angle of 60°. Photoemission (PL) was observed from both the edge and surface directions of the sample as schematically shown

in Fig. 3.2.1c. The edge emission was collected using an aspherical lens and led to a fiber-coupled monochromator equipped with a liquid-N_2-cooled charge-coupled device (CCD). The surface emission was collected from the surface-normal of the top substrate using a 50× objective lens and led to the same fiber-coupled CCD spectrometer. All measurements were conducted at room temperature in ambient air.

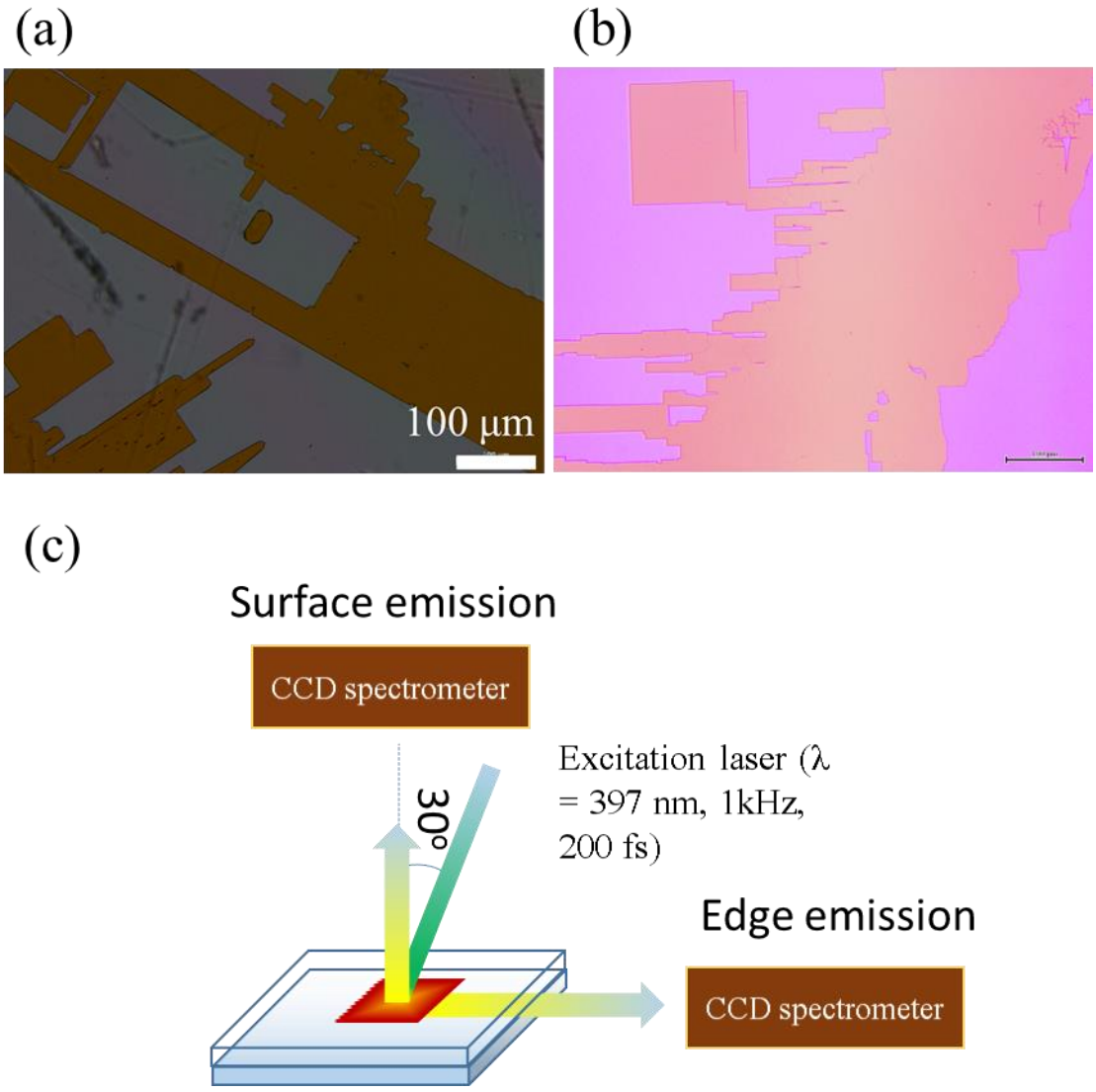

Fig. 3.2.1: *Single-crystal $MAPbBr_3$ prepared by cast-capping method: (a) Stripe-shaped crystals grown between glass/glass substrates and (b) crystals grown between DBR/DBR substrates. (c) Optical configuration in PL measurement setup.*

3.3 Results and Discussion

3.3.1 Characterization of single-crystal $MAPbBr_3$

Fig. 3.3.1 shows the absorption and PL spectrum taken from single-crystal $MAPbBr_3$ grown between glass/glass substrates. The PL peak locates around 2.30 eV and the exciton absorption peak around 2.35 eV although the latter is not clear compared with the former. These excitonic transition peaks indicates a low number of in-gap defect states. According to the previous reports,[13–15] the exciton absorption decreases as the temperature increases and the exciton binding energy accordingly decreases. In comparison with clear band cutoff with no excitonic signature of bulk crystal[16–18] and strong excitonic peak of polycrystalline thin films[8,13–15,19] at room temperature, the absorption spectrum here is close to the results from low-dimensional crystals such as nanoplatelets[20] and nanorods[21] of $MAPbBr_3$. It is suggested that the single-crystal perovskites possess a low exciton binding energy, which might be related to the anisotropic characteristics of excitons in the crystal.

In this study, the DBR substrates used in cast-capping method consist of dielectric multilayers of SiO_2/Ta_2O_5, and their reflectivities (R) are designed to be >90% and >99% by changing the numbers of the multilayers, respectively, at $E = 2.1–2.4$ eV. As a result, the reddish color appears in the DBR/$MAPbBr_3$/DBR samples as shown Fig. 3.2.1b. To

characterize the single-crystal $MAPbBr_3$ prepared by the cast-capping method, one of DBR/$MAPbBr_3$/DBR samples was cleaved to observe by scanning electron microscopy (SEM). The thickness was estimated to be 3.6 μm from the side facet by tilting the sample as shown in Fig. 3.3.2.

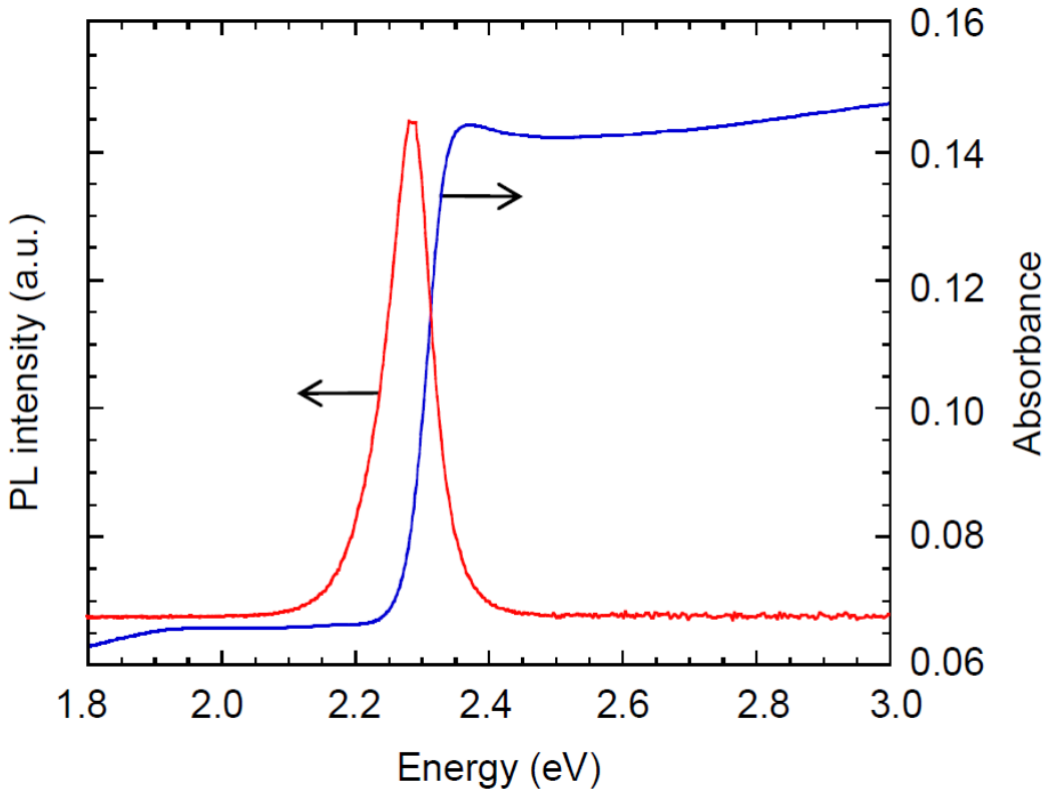

Fig. 3.3.1: *Absorption and PL spectra of single-crystal $MAPbBr_3$ grown between glass/glass substrates.*

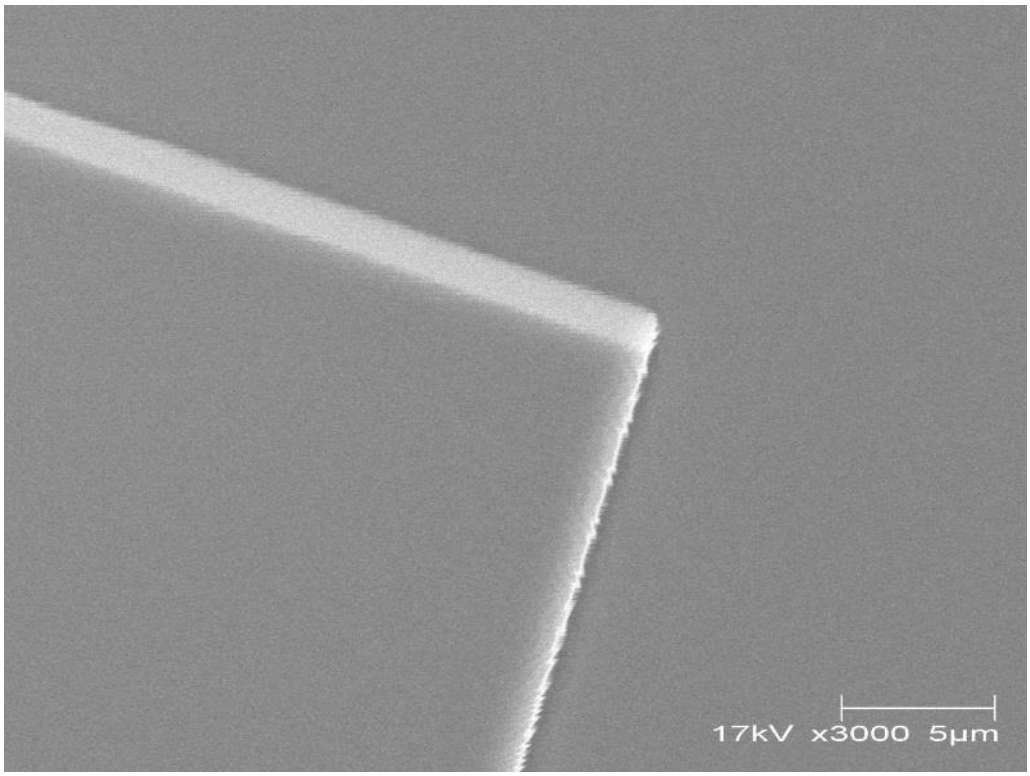

Fig. 3.3.2: *SEM image of $MAPbBr_3$ crystal grown between DBR/DBR substrates.*

3.3.2 Edge-emitting Fabry-Pérot Laser

The excitation-fluence dependence of edge-emitting PL spectra taken from the glass/glass sample is shown in Fig. 3.3.3a. At low fluence below 10 μJ/cm^2, a broad fluorescence band appears at 2.15–2.35 eV which is similar to the case of incoherent excitation shown in Fig. 3.3.3b. With increasing fluence, gain-narrowed emission emerges at 2.20–2.26 eV. The plot of integrated intensity at this energy region as a function of fluence (inset in Fig. 3.3.3a) indicates a nonlinear amplification at a threshold fluence of 12 μJ/cm^2. This threshold is much lower than (350 μJ/cm^2) of ASE taken for

the powder layer of $MAPbBr_3$[22] and also lower than that (30 μJ/cm^2) of WGM lasing in the nanoplatelets of $MAPbBr_3$[23]. Noteworthy, a simultaneous another study of 33.11×31.71×0.31 μm^3 $MAPbBr_3$ microdisk reported that the lasing threshold was of 21μJ/cm^2, which is still 2 time higher in comparison with the present result.[24]

Fig. 3.3.3b shows high-resolution spectra of edge-emitting PL corresponding to Fig. 3.3.3a. The oscillating fringes with a constant energy interval (ΔE) remarkably seen at $E > 2.23$ eV indicates that multimode lasing occurs above the threshold. According to the relation:

$$\Delta E = \frac{hc}{2n_{\text{eff}} L} \qquad (1)$$

where h is the Planck constant and c is the speed of light. The resonator length L is estimated to be ~34 μm using an average value of the effective refractive index $n_{\text{eff}} = 4.5$ reported for self-assembled $MAPbBr_3$ microdisks.[23] This length is almost comparable to the width of strip-shaped part growing out of the planar crystal as shown in Fig. 3.2.1a. As the results, this observed edge-emitting laser is ascribed to Fabry-Pérot (F-P) resonation between parallel side facets of the strip-shaped part in the crystal. A Q factor of this F-P resonator is estimated from the linewidth at half maximum (ΔE_{FWHM}) of the lasing peak at $E = 2.235$ eV, resulting in $Q_{\text{exp}} = E/\Delta E_{\text{FWHM}} = 1470$. This value in the lasing regime is similar with that of 1460 in $MAPbBr_3$ microdisk lasing[24], but it is noteworthy

one order as high as the theoretical value (= 148) in the spontaneous regime calculated from the following equation:

$$Q = \frac{n_{\text{eff}}\,\omega_0}{(c/L)\ln(1/R_1R_2)} \qquad (2)$$

where ω_0 is the peak frequency, R_1 and R_2 are the reflectivity at the side facets of the strip-shaped crystal of $MAPbBr_3$. The R_1 and R_2 are estimated to be 0.155 following $R = (n_1 - n_0)^2/(n_1 + n_0)^2$ where n_0 (= 1) is the phase refractive index of air and n_1 (= 2.3) is that reported for MABr:$PbBr_2$.[25] Although the F-P mode peaks are not well recognized in the spontaneous regime below the threshold, this increment of the lasing Q value clearly demonstrates amplification by the stimulated emission process.

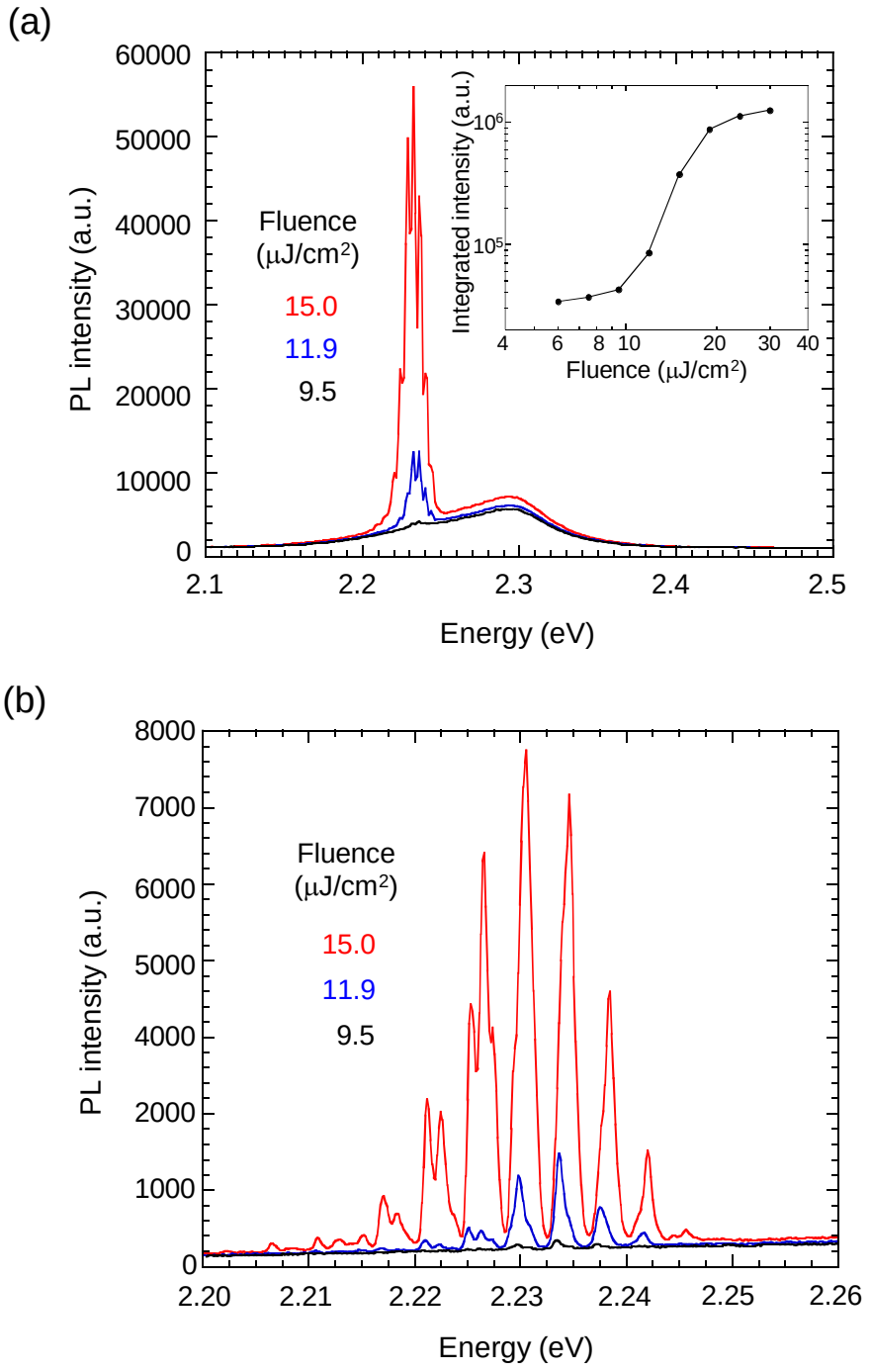

Fig. 3.3.3: *a) Excitation-fluence dependence of edge-emitting PL spectra taken form strip-shaped $MAPbBr_3$ grown between glass/glass subtrates. The inset shows PL intensity integrated at E = 2.20 – 2.26 eV as a function of excitation fluence. b) High-resolution spectra at E = 2.20 – 2.26 eV corresponding to the edge-emitting PL spectra in (a).*

3.3.3 Vertical-cavity surface-emitting Laser (VCSEL)

Next, surface-emitting properties were investigated using the DBR/DBR samples in which a large $MAPbBr_3$ crystal grows in a single domain of ~1 mm (see inset image in Fig. 3.3.4b). Figure 3.3.4a shows fluence dependence of PL spectra taken from the surface-normal of the top DBR substrate. In the stop-band of the DBR (R > 90% at E = 2.1 - 2.4 eV), an intense emission peak appears at E = 2.237 eV accompanying a weak emission at E = 2.289 eV. Assuming that the ΔE between these peaks corresponds to a mode interval, the cavity thickness L between the top and bottom DBRs, is estimated from equation (1) to be ~2.7 μm. As is shown in the inset of Fig. 3.3.4a, the integrated intensity of the former peak nonlinearly increases above an excitation threshold of 26 $\mu J/cm^2$. This threshold for vertical-cavity surface-emitting laser (VCSEL) is remarkably larger than that of the edge-emitting laser described in the previous section.

Furthermore, the linewidth of this VCSEL peak (ΔE_{FWHM} = 4.9 meV) is larger than that of the edge-emitting laser peak (ΔE_{FWHM} = 1.5 meV) in Fig. 3.3.3(b). As a result, the Q value of this DBR/DBR cavity is estimated to be 454 which is much lower than that obtained for the edge-emitting laser (Q = 1470) even though the reflectivity of the DBR mirror (R > 90%) is much higher than that of the self-formed side-facets of the strip-

shaped crystal (R = 15.5%). This Q value estimated for the VCSEL is almost comparable to a theoretical value (Q = 375) in the spontaneous regime calculated from equation (2).

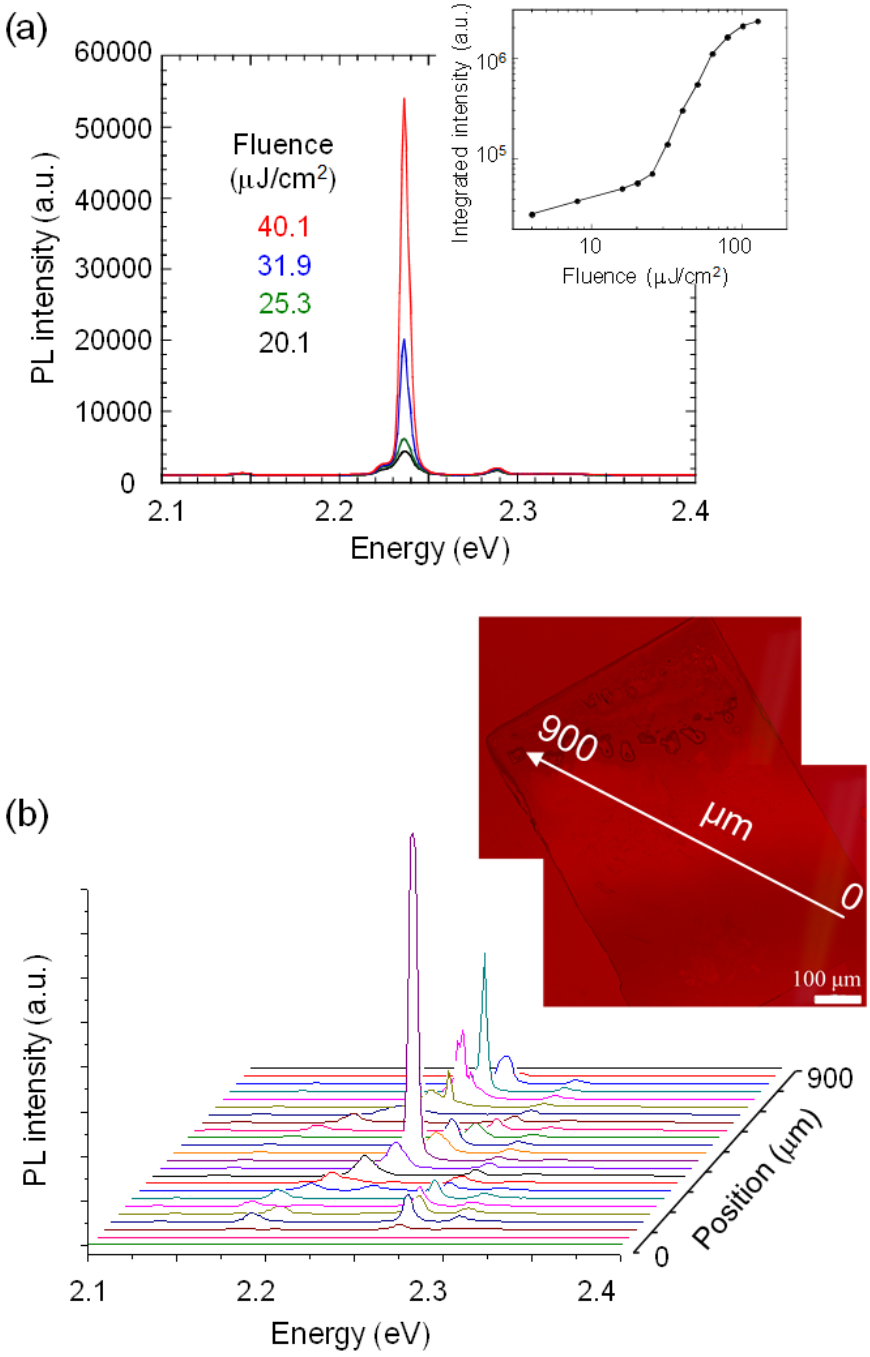

Fig. 3.3.4: *(a) Excitation density dependence of PL spectra taken from planar $MAPbBr_3$ crystal grown between DBR/DBR substrates. The inset shows integrated PL intensity of the emission peak at E = 2.237 eV as a function of excitation density. (b) Spectral change in surface-emitting laser taken with shifting excitation positions along the arrow shown in the inset micrograph.*

Such a lower lasing performance of the VCSEL compared to the edge-emitting F-P laser is attributed to a slight gradient of the crystal thickness sandwiched between the top and bottom DBR substrates. Fig. 3.3.4b shows a spectral change of VCSEL taken from the large planar crystal in the DBR/DBR cavity in which the position of excitation spot ($\sim 25 \times 60\ \mu m^2$) is moved from 0 to 900 μm along the arrow in the inset micrograph. As the excitation spot is shifted, two prominent lasing modes always appear while their mode interval ΔE gradually changes from 32.0 meV (minimum) to 94.7 meV (maximum). This mode-interval change corresponds to a gradient of the crystal thickness (i.e. the vertical cavity length) in a range of L = 1.46 – 4.31 μm, resulting in a thickness gradient of approximately 0.46° ($\tan\theta$ = ~0.008). This inconstant vertical cavity length deteriorates the Q factor of the VCSEL. Therefore, the Q value is considerably reduced as compared to that of the edge-emitting laser which is based on the F-A resonation of the strip-shaped crystal. It demonstrates that the self-formed side-facets of the strip-shaped crystal function as high-quality parallel mirrors owing to the cubic nature of the $MAPbBr_3$ crystal.

3.3.4 Simultaneous observation of edge- and surface-emitting lasers

Such a better performance of the edge-emitting laser is also confirmed by simultaneous detection of both the edge-emitting laser and VCSEL from the $MAPbBr_3$

crystal grown between the DBR/DBR substrates. Figure 3.3.5 shows an excitation density dependence of PL spectra taken from the surface-normal direction of the planar crystal sandwiched between the DBR/DBR substrates shown in Fig. 3.3.1b. At low excitation density below 20 μJ/cm^2, emission peaks assigned to surface-emitting vertical-cavity modes appear at 2.18 and 2.30 eV. With increasing excitation density, multiple peaks emerge at E = 2.22 – 2.28 eV. This multimode emission is ascribed to the edge-emitting F-P laser which occurs at a strip-shaped part of the crystal. From the mode interval (ΔE_{FWHM} = ~7 meV) between these multimode peaks, the lateral cavity length for this F-P lasing is estimated to be L = ~20 μm. Such multimode emission was not observed in the spontaneous regime since the edge emission cannot be collected in the surface-normal direction. However, once the edge emission lases, its scattered signals can be detected even in the surface-normal collection. Edge-emitting intensities of the lasing peak at E = 2.258 eV and integrated intensities of the surface-emitting peaks at E = 2.18 and 2.30 eV are plotted as a function of excitation density in the inset of Fig. 3.3.5. The nonlinear increase of the edge-emitting intensity indicates its lasing threshold of 24 μJ/cm^2. By contrast, both surface-emitting intensities linearly increase in the measured excitation density range suggesting that the surface emission is still in the spontaneous regime and their VCSEL thresholds are higher than that of the edge-emitting laser.

The reason for the lower performance in the VCSEL is again attributed to inhomogeneous thickness.[26] In the present cast-capping method, the top substrate is just faced down to the precursor solution and it attaches to the bottom substrate with a surface tension of the solution. The crystals growth proceeds upon solvent evaporation from the sample edge, therefore the uniformity of crystal thickness depends on the evaporation speed as well as the flatness of substrate surface. The estimated thickness gradient ($\tan\theta$ = 0.008) in Fig. 3.3.4b may cause a considerable reduction of the Q value resulting in higher VCSEL threshold in comparison to the edge-emitting laser.

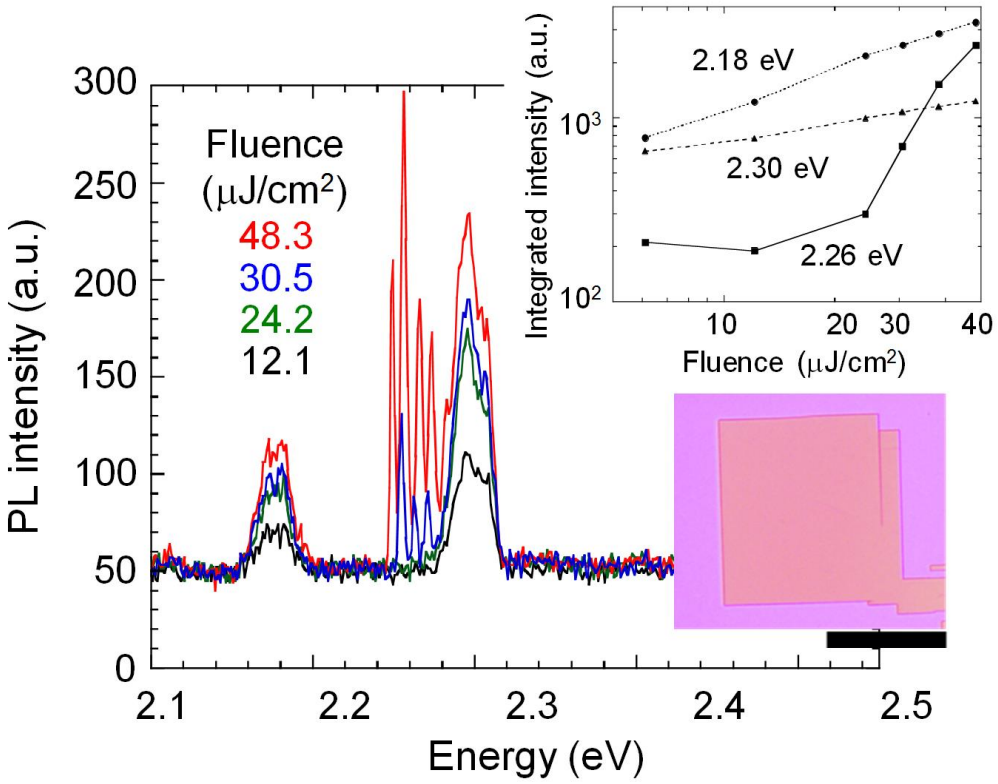

Fig. 3.3.5: *Excitation density dependence of PL spectra taken from surface-normal of the planar crystal (the bar = 100 μm). The inset shows integrated PL intensities of the edge-emitting multimode peaks at E = 2.258 eV and the surface-emission peaks at 2.18 and 2.30 eV as a function of excitation density*

3.4 Summary

In summary, this chapter investigated the lasing from large-size single-domain crystals of $MAPbBr_3$ prepared by the cast-capping method. Under optical pumping, edge-emitting laser was achieved based on F-P resonation in the lateral cavity of strip-shaped crystals grown between the glass/glass substrate. When the planar $MAPbBr_3$ crystal was grown between the DBR/DBR substrates, VCSEL was successfully observed in the surface-normal direction. However, the lasing characteristics of the VCSEL showed higher excitation thresholds and lower Q values as compared to those of edge-emitting F-P laser. The lower lasing performance of VCSEL was ascribed to the thickness gradient of the planar crystal between the top and bottom DBRs prepared by the present cast-capping method. On the other hand, the better performance of the edge-emitting F-P laser with lower thresholds and higher Q values resulted from the well-shaped side-facets of the strip-shaped crystal acting as self-formed F-P mirrors. In order to improve the VCSEL performance, the thickness uniformity must be precisely regulated. For this purpose, it is required to use a thin spacer with extremely flat top/bottom substrates in the future experiments.

References

1. Nguyen, V. C. *et al.* Optically pumped lasing in simple solution-processed single crystals of organometal halide perovskites. *Appl. Phys. Lett.* **108,** 261105 (2016).
2. Sutherland, B. R. & Sargent, E. H. Perovskite photonic sources. *Nat. Photonics* **10,** 295–302 (2016).
3. Green, M. A. & Bein, T. Photovoltaics: Perovskite cells charge forward. *Nat. Mater.* **14,** 559–561 (2015).
4. Egger, D. A. *et al.* Perovskite Solar Cells: Do We Know What We Do Not Know? *J. Phys. Chem. Lett.* **6,** 279–282 (2015).
5. Park, N. *et al.* Towards stable and commercially available perovskite solar cells. *Nat. Energy,* 16152 (2016). doi:10.1038/NENERGY.2016.152
6. Yablonovitch, E. Lead halides join the top optoelectronic league. *Science* **351,** 1401–1401 (2016).
7. Mitzi, D. B. *Synthesis, Structure, and Properties of Organic-Inorganic Perovskites and Related Materials*. (John Wiley & Sons, Inc., 1999).
8. Bade, S. G. R. *et al.* Fully Printed Halide Perovskite Light-Emitting Diodes with Silver Nanowire Electrodes. *ACS Nano* **10,** 1795–1801 (2015).
9. Bush, K. A. *et al.* 23.6%-efficient monolithic perovskite/silicon tandem solar cells with improved stability. *Nat. Energy* **2,** 17009 (2017).
10. Xing, G. *et al.* Low-temperature solution-processed wavelength-tunable perovskites for lasing. *Nat. Mater.* **13,** 476–480 (2014).
11. Zhang, Q. *et al.* Room-Temperature Near-Infrared High‐Q Perovskite Whispering-Gallery Planar Nanolasers. *Nano Lett.* **14,** 5995–6001 (2014).
12. Zhu, H. *et al.* Lead halide perovskite nanowire lasers with low lasing thresholds and high quality factors. *Nat. Mater.* **14,** 636–642 (2015).
13. Sestu, N. *et al.* Absorption F-Sum Rule for the Exciton Binding Energy in Methylammonium Lead Halide Perovskites. *J. Phys. Chem. Lett.* **6,** 4566–4572 (2015).
14. Soufiani, A. M. *et al.* Polaronic exciton binding energy in iodide and bromide organic-inorganic lead halide perovskites. *Appl. Phys. Lett.* **107,** 23192 (2015).
15. Saba, M. *et al.* Excited State Properties of Hybrid Perovskites. *Acc. Chem. Res.* **49,** 166–173 (2016).
16. Shi, D. *et al.* Low trap-state density and long carrier diffusion in organolead trihalide perovskite single crystals. *Science* **347,** 519–522 (2015).
17. Saidaminov, M. I. *et al.* High-quality bulk hybrid perovskite single crystals within

minutes by inverse temperature crystallization. *Nat. Commun.* **6,** 7586 (2015).

18. Fang, Y. *et al.* Highly narrowband perovskite single-crystal photodetectors enabled by surface-charge recombination. *Nat. Photonics* **9,** 679–686 (2015).
19. Li, G. *et al.* Efficient Light-Emitting Diodes Based on Nanocrystalline Perovskite in a Dielectric Polymer Matrix. *Nano Lett.* **15,** 2640–2644 (2015).
20. Ha, S. T. *et al.* Synthesis of Organic-Inorganic Lead Halide Perovskite Nanoplatelets: Towards High-Performance Perovskite Solar Cells and Optoelectronic Devices. *Adv. Opt. Mater.* **2,** 838–844 (2014).
21. Wong, A. B. *et al.* Growth and Anion Exchange Conversion of $CH_3NH_3PbX_3$ Nanorod Arrays for Light-Emitting Diodes. *Nano Lett.* **15,** 5519–5524 (2015).
22. Priante, D. *et al.* The recombination mechanisms leading to amplified spontaneous emission at the true-green wavelength in $CH_3NH_3PbBr_3$ perovskites. *Appl. Phys. Lett.* **106,** 81902 (2015).
23. Wang, K. *et al.* Unidirectional Lasing Emissions from $CH_3NH_3PbBr_3$ Perovskite Microdisks. *ACS Photonics* **3,** 1125–1130 (2016).
24. Sasaki, F. *et al.* Optical pumped lasing in solution processed perovskite semiconducting materials: Self- assembled microdisk lasing. *Jpn. J. Appl. Phys.* **55,** 04ES02 (2016).
25. Leguy, A. M. A. *et al.* Experimental and theoretical optical properties of methylammonium lead halide perovskites. *Nanoscale* **8,** 6317–6327 (2016).
26. Jurow, M. J. *et al.* Tunable Anisotropic Photon Emission from Self-Organized $CsPbBr_3$ Perovskite Nanocrystals. *Nanolett.* **17,** 4534-4540 (2017).

Chapter 4
Electroluminescence of single-crystal $MAPbBr_3$ prepared by cast-capping method

Perovskites attract much attention in solution-processable flexible optoelectronics since their devices have been reaching the highest photovoltaic efficiencies. Their unique physical properties also make them promising candidate for applications in light-emitting devices. However, the exciton and carrier behaviors in perovskites are still under the debate. In this chapter, electroluminescence (EL) properties and its mechanism are investigated for single-crystal $MAPbBr_3$ in simple ITO/$MAPbBr_3$/ITO devices prepared by the cast-capping method. Although it is very simple structure without charge transport layers which are incorporated in conventional OLEDs, the ITO/$MAPbBr_3$/ITO devices emitted pure green luminescence with FWHM of ~20 nm at applied bias voltages above 2 V. Note that EL and its blinking were observed at the edge and corner of single-crystal $MAPbBr_3$. These investigations provide a new insight into the recombination processes in the perovskite crystals to improving the performance of perovskite light-emitting diodes (PeLEDs)[1].

4.1 Introduction

Organic LEDs (OLEDs) and inorganic quantum dot LEDs (QLEDs) have been extensively investigated in recent years and some of them have been already commercialized. However, they have revealed some issues need to improve such as color purity and ionization energy (QLEDs). As discussed in Chapter 1, the methylammonium lead halide perovskites ($MAPbX_3$) consist of the MA cation and $[PbX_6]^{4-}$ octahedral, which share corners in all three orthogonal direction to form the infinite three-dimensional $[PbX_3]^-$ frame work.[2–4] Because of the dielectric constant difference between organic and inorganic components in the crystals, the exciton was confined in the inorganic layer resulting in a high color purity (FWHM ~ 20 nm for $MAPbBr_3$) irrespective of the crystal size.[3,4] Along with its long carrier diffusion length contributing in high-efficiency solar cells, these properties have made perovskites a top candidate material for next generation LEDs.[5] Recently, a high external quantum efficiency (EQE) up to 10% has been achieved.[6,7] In these reports, the authors showed that the reduction of grain sizes to confine the excitons enhances the radiative recombination. Another study has also indicated that the passivation layer can coordinate with the under-coordinated lead ions, and the additive material then improves the performance of PeLED.[8] Noteworthy, all of these studies have been carried out by using nanocrystalline thin films

prepared by the spin-coating method.

In this chapter, electroluminescence (EL) properties of perovskites are contrastingly investigated for single-crystal $MAPbBr_3$ prepared by the cast-capping method. Very simple devices with the ITO/$MAPbBr_3$/ITO structure can show intrinsic excitons and carrier behaviors inside the crystals. In addition, the effect of a hole injection interlayer of PEDOT:PSS and pre-casting of a MABr layer cast-capping method on the EL behaviors are investigated.

4.2 Experimental

In conventional OLEDs, beside top/bottom electrodes and an active organic layer, additive layers are used for injection of electrons and holes to the emissive layer where the excitons are formed. In this study, the EL behaviors were investigated by eliminating those charge transport layers to prevent the effect of interlayer between perovskites and those layers by building a simple ITO/$MAPbBr_3$/ITO structure as shown in Fig. 4.2.1. Following the experiments presented in chapter 2, the single-crystal $MAPbBr_3$ was formed in cavity between ITO substrates as shown in Fig. 4.2.1.

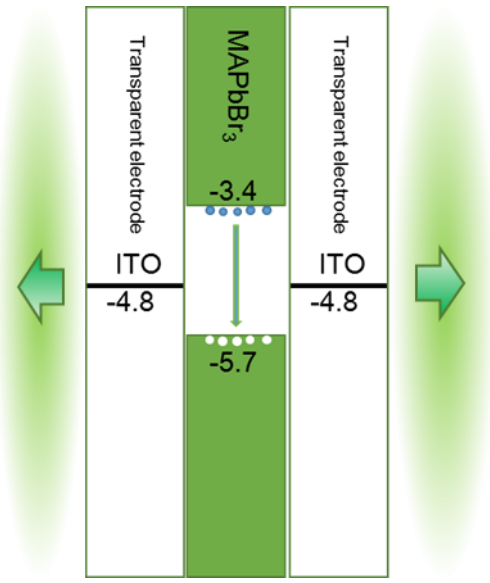

Fig. 4.2.1: *Schematic of simple ITO/$MAPbBr_3$/ITO device and its energy band diagram.*

Some representative samples were cleaved into each ITO substrate then analyzed by an X-Ray diffractometer (Rigaku, RINT-TTRIII/NM). A UV/VIS spectrophotometer (V-530, Jasco) was used to analyze electronic characteristics. To measure EL and PL, a multi-channel spectrometer (Hamamatsu photonics PMA-12) was connected to a microscope system (Olympus BX-51). To measure EL and I-V characteristics of ITO/$MAPbBr_3$/ITO, a conductive past (DOTITE D-500, Fujikura Kasei Co., Ltd) was used to contact the ITO electrodes with a copper wire before connecting them to a source/measure unit (Agilent B2902A). All these measurements were carried out in air at room temperature.

4.3 Results and Discussion

4.3.1 Electroluminescence of single-crystal $MAPbBr_3$

In this study, a DC power supply was used to electrically inject carriers to single-crystal $MAPbBr_3$ through ITO electrodes. At a low bias voltage below 2 V, the carriers are hardly injected because of high energy barriers between the ITO and perovskite layer, consequently EL was not observed. However, when the bias voltage is increased higher than 2 V, EL starts to be detected remarkably at the crystal edges and corners. As shown in Fig. 4.3.1a-d, the luminescence gradually increases when the bias voltage is increased from 2 V to 4 V. In three cycles scan from 0 to 4 V, the forward and backward currents gradually decrease while their hysteresis is kept quite small (Fig. 4.3.1e). This current decrease may be caused by a damage in the crystal due to Joule heating. When the applied voltage was increased higher than 10 V, the $MAPbBr_3$ crystals were visibly destroyed.

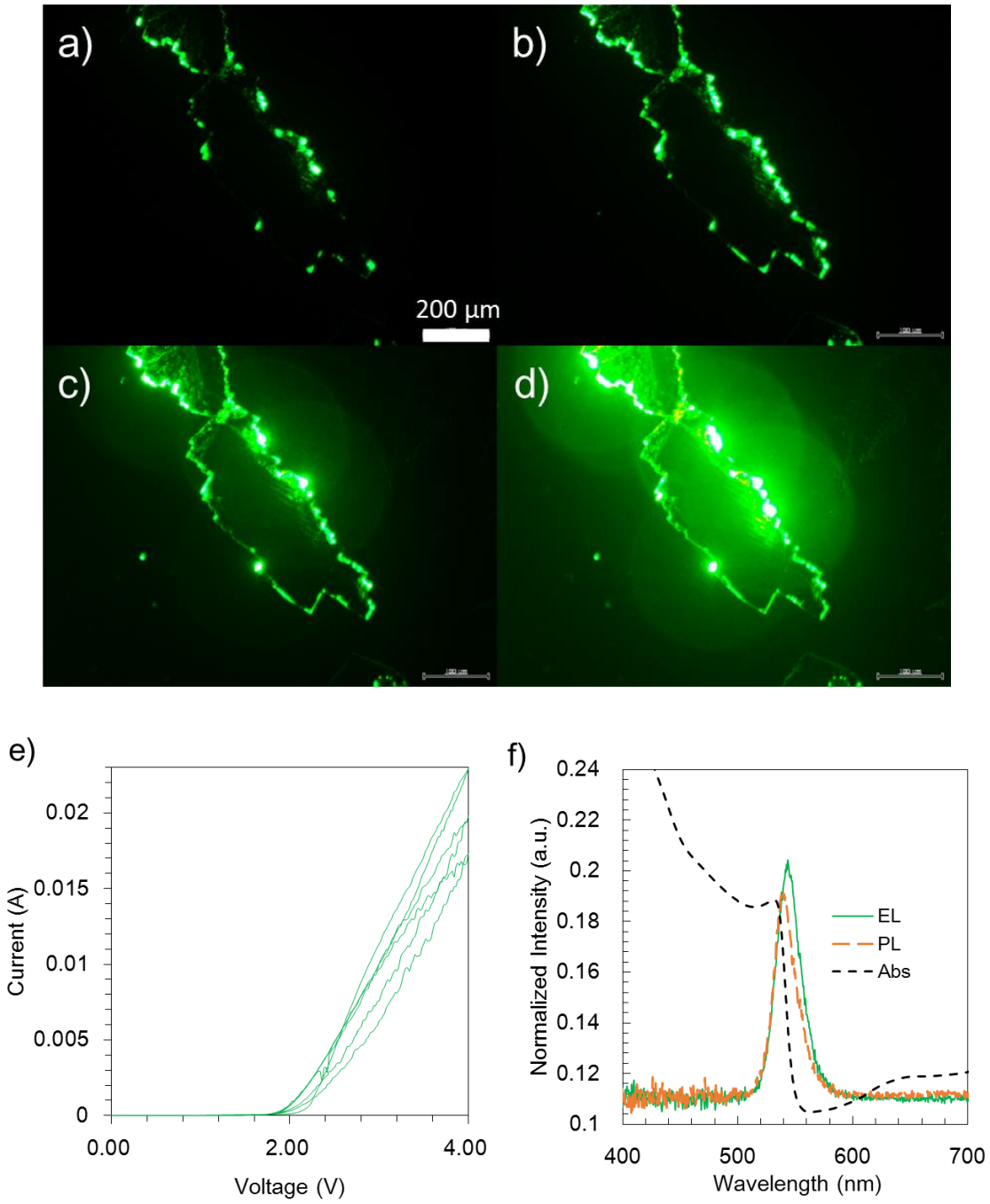

Fig. 4.3.1: *a-d) Pure green luminescence of single-crystal $MAPbBr_3$ in the PeLED with increasing bias voltages from 2 to 4 V. e) Forward and backward I-V curves measured in 3 cycles. f) Absorption (black, dashed), PL (orange, dashed) and EL (green, solid) spectra of the PeLED device.*

In the present study, different from the previously reported PeLEDs, intrinsic EL, PL and absorption spectra of $MAPbBr_3$ can be investigated in the crystal cavity between the transparent ITO substrates without any other layers as shown in Fig. 4.3.1f. The weak peak in the absorption spectrum near the bandgap corresponds to excitonic transition in single-crystal $MAPbBr_3$as discussed in Chapter 2, indicating that there are a low number of in-gap defects in the $MAPbBr_3$ crystals. This excitonic band gap, ~2.25 eV, is comparable with those in the bulk crystal (2.21 eV)[9] and crystalline thin films (2.30 eV)[10] in other reports. The PL spectrum shows a peak at ~ 540 nm with FWHM of ~ 19 nm. Note that there is no hole and electron transport layer in the present device. Therefore, the interfaces between the perovskite and these layers are eliminated. As a result, these characteristic come from intrinsic properties of the single-crystal $MAPbBr_3$ in the devices.

Z. K. Tan et al. reported the blue-shifted EL in comparison with PL arising from interaction between the transport layers and perovskite thin film.[11] On the contrary, Fig. 4.3.1f indicates slightly red-shifted EL peak about 0.02 eV in comparison with PL. In agreement with the study by D. S. Ginger et al, the red-shifted EL might come from the shallow trapping level formed at the crystal edges and corners.[12] The large carrier diffusion length in single-crystal perovskite resulting from low defect density reduces non-radiative trapping paths.[9,11,13] However, some of previous studies indicate that the

radiative recombination is enhanced when the grain size is reduced although the number of defects in the perovskite thin films is increased.[6,7] Furthermore, the PL quantum yields of perovskite is efficiently improved when the film surface is passivated with a ligand.[12,14] As a result, it suggest that the carriers are diffused and accumulated at the grain boundaries and surfaces, subsequently, excitons are generated there at high probability. Therefore, the edges and corners of single-crystal $MAPbBr_3$ might become dominant sites of radiative recombination.

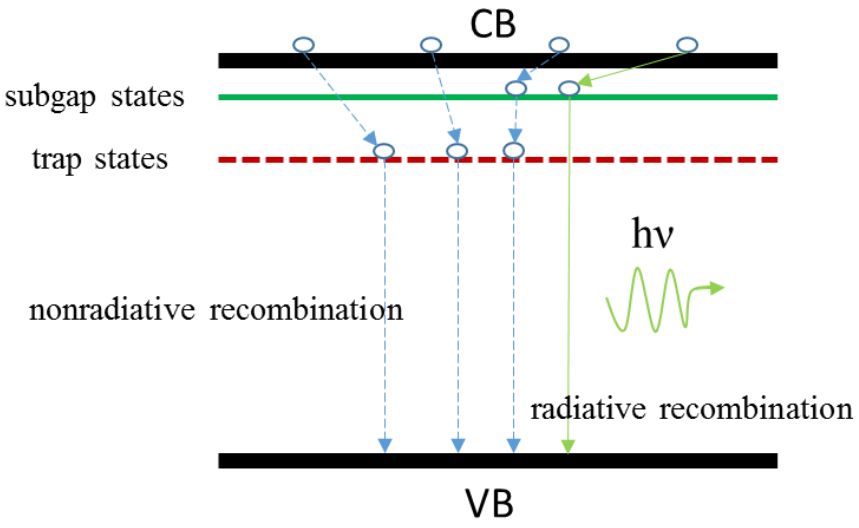

Fig. 4.3.2: *Proposed emission mechanism of single-crystal $MAPbBr_3$ in PeLED.*

The proposed LED operation mechanisms can be represented as show in Fig. 4.3.2. Under application of bias voltages, there is a sub-gap states existing at the crystal edge, which are attributed to the red-shifted EL observed in Fig. 4.3.1f. Note that the carrier

trap states might be also concentrated at the edge and corner of the single crystal where chemical defects such as uncoordinated Pb atoms, ion vacancies and mobile Br ions may predominantly exist. The excitons are trapped in the radiative sub-gap states to emit photons or quenched by non-radiative recombination paths by carrier traps. As a results, the EL blinking was observed in the single crystals as shown in Fig. 4.3.3. Similarly, PL blinking[15–18] as well as EL blinking[8,19] were observed in nanocrystal perovskites and their blinking mechanisms are proposed:

a) The non-radiative Auger recombination of excitons by trapped electrons or holes.

b) The intermittent quenching of excitons by the traps with the chemical defects in the nanocrystals.

In the present devices, PL was observed in the crystal surface in contact with ITO substrates and there was no PL blinking. Therefore, the excitons quenching by Auger effect might be negligible due to low surface trap states. In the case of EL when the carriers are injected under application of bias voltages to ITO electrodes, the interface between the $MAPbBr_3$ and ITO surfaces is not capable for radiative recombination. As a result, the intermittent quenching of excitons by non-radiative carrier traps at the crystal edges and corners of single-crystal $MAPbBr_3$ is a more plausible reason for the EL blinking.

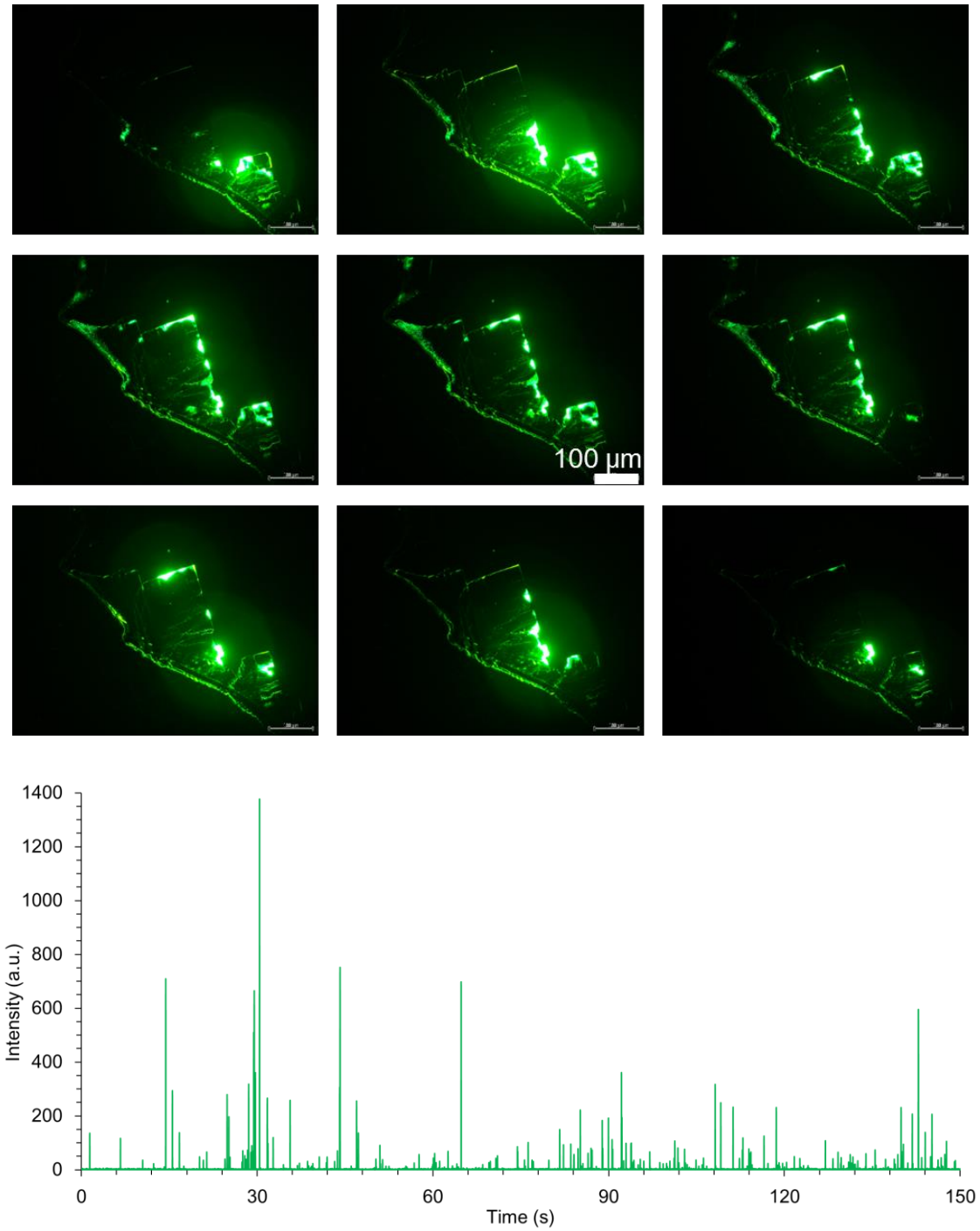

Fig. 4.3.3: *Optical micrograph of single-crystal $MAPbBr_3$ indicating "on" and "off" of emission at bias voltage of 4 V and time profile showing EL blinking measured at λ = 549.4 nm.*

4.3.2 Enhanced optical properties of single-crystal $MAPbBr_3$ by passivating materials

As well known, PEDOT:PSS is widely used as hole injection layer in OLEDs, which is also commonly used in PeLEDs. Here, the effect of this layer on luminescence by PL measurements, to further investigate the performance of the present devices. The cast-capping method was employed to fabricate ITO/PEDOT:PSS/$MAPbBr_3$/PEDOT:PSS/ITO devices. Firstly, PEDOT:PSS was spin-coated on ITO substrates. After dried at 120°C in a glove box purged with nitrogen, these substrates were provided to the cast-capping method with the same precursor solution as used in the fabrication of the ITO/$MAPbBr_3$/ITO devices. Furthermore, the MABr was also used as a passive layer between single-crystal $MAPbBr_3$ and ITO surface to improve the performance of PeLEDs. MABr dissolved in DMF was spin-coated on the ITO substrates and dried in vacuum at room temperature for 24 hours. These substrates were used in the cast-capping method to prepare single-crystal $MAPbBr_3$.

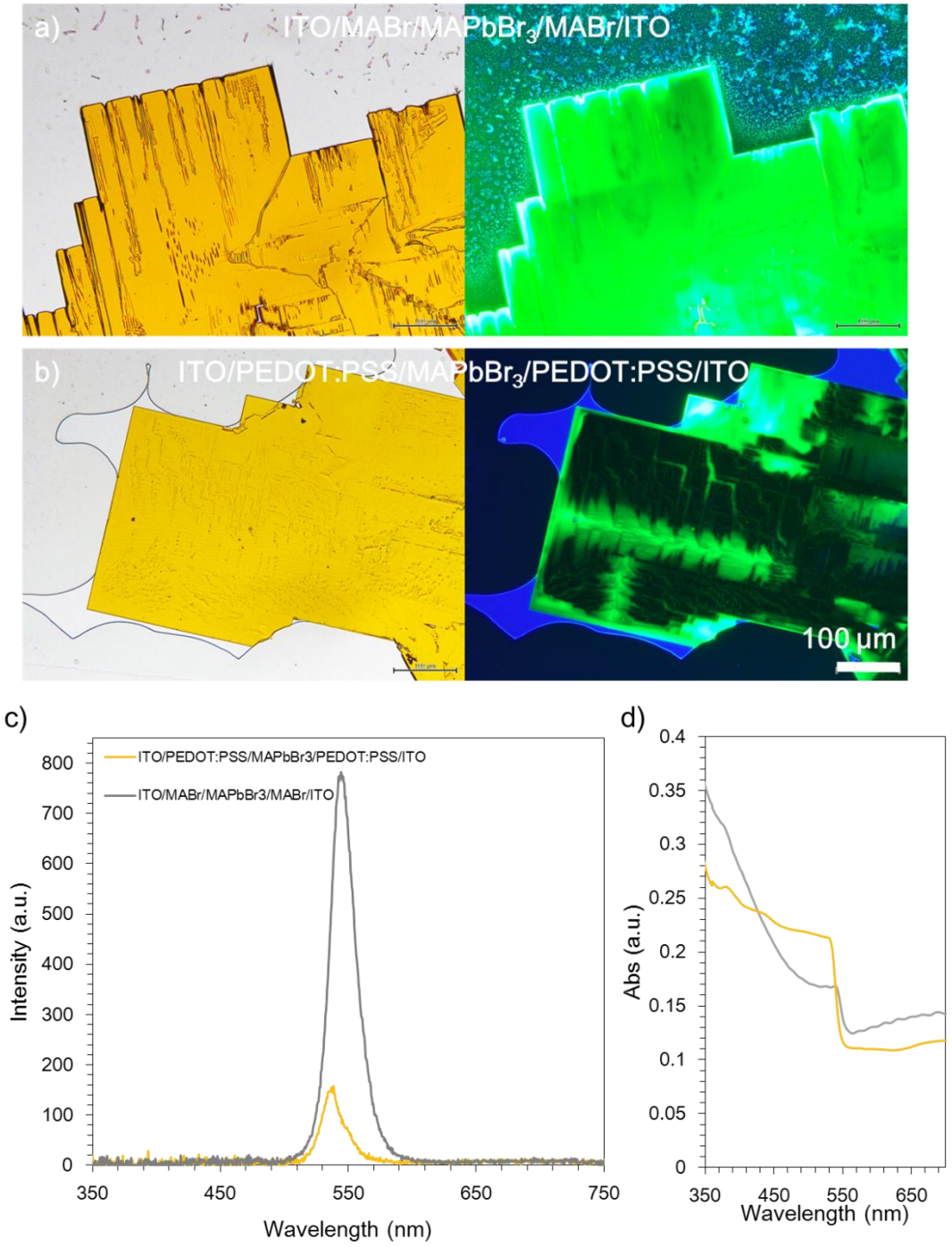

Fig 4.3.4: *Optical micrographs of a) ITO/MABr/MAPbBr₃/MABr/ITO and b) ITO/PEDOT:PSS/MAPbBr₃/PEDOT:PSS/ITO prepared by the cast-capping method. Their PL and absorption spectra are shown in (c)and (d), respectively.*

Figures 4.3.4a-b show optical micrographs of ITO/MABr/$MAPbBr_3$/MABr/ITO and ITO/PEDOT:PSS/$MAPbBr_3$/PEDOT:PSS/ITO devices, respectively, under white (left) illumination, and their fluorescence micrographs under UV excitation (right) . Note that MABr and PEDOT:PSS can be dissolved into perovskite precursor solution during crystal formation in the cast-capping method. As shown in Fig. 4.3.4a, bright emission was observed homogeneously in the whole crystal area in the MABr/$MAPbBr_3$ sample. On the other hand, in the $MAPbBr_3$/PEDOT:PSS sample, PL was localized remarkable at the crystal edges and corners as well as defects probably existing inside the crystal. It suggests that the excitons are trapped there, then emit light by radiative recombination via the radiative sub-gap states or quenched by the non-radiative carrier traps at defect site. Noteworthy, the latter quenching at the interface between the $MAPbBr_3$ crystal surface and ITO electrodes are remarkably reduced by pretreating the ITO surface with MABr in the ITO/MABr/$MAPbBr_3$/MABr/ITO device.

PL and absorption measurements were carried out to compare their exciton generation and recombination properties in the $MAPbBr_3$ crystals. As shown in Fig. 4.3.4c, the PL intensity in the $MAPbBr_3$/PEDOT:PSS sample (yellow) is very weak in comparison with the MABr/$MAPbBr_3$ sample (gray). Both these samples show clear band edge cutoff with excitonic signatures (Fig. 4.3.4d), suggesting a minimal number of in-

gap defect states in the PEDOT:PSS/$MAPbBr_3$ and MABr/$MAPbBr_3$ interlayers. Although time-resolved PL measurements were not carried out in this study, the previous studies reported that “bright” and “dark” regions were ascribed correspondingly to the fast and slow decay, respectively.[12,14,16,20,21] As a result, the PEDOT:PSS/$MAPbBr_3$ interlayer dominates the non-radiative pathways and the MABr passivation layer can enhance the radiative recombination in LED devices. These findings are very interesting in comparison with the previous studies introducing a passive layer such as pyridine, long-chain halide, polyethylenimine and ethylenediamine to remediate the non-radiative defects in the polycrystalline perovskite thin films,[8,12] to further elucidate the emission mechanism and to improve the device performance.

4.4 Summary

In this chapter, EL behaviors were characterized for the simple LED with single-crystal $MAPbBr_3$. The edge and blinking EL suggests that the carriers are diffused and considerably accumulated at the crystal edges and corners then generate excitons there. These excitons are probably trapped by chemical defects consisting of uncoordinated Pb atoms and mobile Br ions. Some of them surviving from non-radiative quenching contribute to radiative emission through the sub-gap states. Noteworthy, the non-radiative quenching occurring at the interface between the $MAPbBr_3$ crystal surface and ITO substrate can be suppressed by passivating effect of pre-depositing MABr layer. It suggests that the EL can be obtained from the entire surface of the single-crystal perovskites and the EL blinking could be avoided by using this passivation technique. The present successful fabrication of those simple PeLEDs demonstrates that the cast-capping method can be widely applied to other optoelectronic devices with perovskites.

References

1. Nguyen, V. C. *et al.* Single-crystal perovskite $CH_3NH_3PbBr_3$ prepared by cast-capping method for light-emitting diodes. *Jpn. J. Appl. Phys.* **57**, 04FL10 (2018).
2. Stoumpos, C. C. & Kanatzidis, M. G. The Renaissance of Halide Perovskites and Their Evolution as Emerging Semiconductors. *Acc. Chem. Res.* **48,** 2791–2802 (2015).
3. Saparov, B. & Mitzi, D. B. Organic−Inorganic Perovskites: Structural Versatility for Functional Materials Design. *Chem. Rev.* **116,** 4558–4596 (2016).
4. Kim, Y. H. *et al.* Multicolored organic/inorganic hybrid perovskite light-emitting diodes. *Adv. Mater.* **27,** 1248–1254 (2015).
5. Veldhuis, S. A. *et al.* Perovskite Materials for Light-Emitting Diodes and Lasers. *Adv. Mater.* **28,** 6804–6834 (2016).
6. Cho, H. *et al.* Overcoming the electroluminescence efficiency limitations of perovskite light-emitting diodes. *Science* **350,** 1222–1225 (2015).
7. Xiao, Z. *et al.* Efficient perovskite light-emitting diodes featuring nanometre-sized crystallites. *Nat. Photonics* **11,** 108–115 (2017).
8. Lee, S. *et al.* Amine-Based Passivating Materials for Enhanced Optical Properties and Performance of Organic−Inorganic Perovskites in Light-Emitting Diodes. *J. Phys. Chem. Lett.* **8,** 1784–1792 (2017).
9. Shi, D. *et al.* Low trap-state density and long carrier diffusion in organolead trihalide perovskite single crystals. *Science* **347,** 519–522 (2015).
10. Bade, S. G. R. *et al.* Fully Printed Halide Perovskite Light-Emitting Diodes with Silver Nanowire Electrodes. *ACS Nano* **10,** 1795–1801 (2015).
11. Tan, Z.-K. *et al.* Bright light-emitting diodes based on organometal halide perovskite. *Nat. Nanotechnol.* **9,** 687–692 (2014).
12. DeQuilettes, D. W. *et al.* Impact of microstructure on local carrier lifetime in perovskite solar cells. *Science* **348,** 683–686 (2015).
13. Saidaminov, M. I. *et al.* High-quality bulk hybrid perovskite single crystals within minutes by inverse temperature crystallization. *Nat. Commun.* **6,** 7586 (2015).
14. Stranks, S. D. Nonradiative Losses in Metal Halide Perovskites. *ACS Energy Lett.* **2,** 1515–1525 (2017).
15. Tachikawa, T., Karimata, I. & Kobori, Y. Surface Charge Trapping in Organolead Halide Perovskites Explored by Single-Particle Photoluminescence Imaging. *J. Phys. Chem. Lett.* **6,** 3195–3201 (2015).
16. Wen, X. *et al.* Morphology and Carrier Extraction Study of Organic − Inorganic

Metal Halide Perovskite by One- and Two-Photon Fluorescence Microscopy. *J. Phys. Chem. Lett.* **5,** 3849–3853 (2014).

17. Tian, Y. *et al.* Giant Photoluminescence Blinking of Perovskite Nanocrystals Reveals Single-Trap Control of Luminescence. *Nano Lett.* **15,** 1603–1608 (2015).
18. Yarita, N. *et al.* Dynamics of Charged Excitons and Biexcitons in CsPbBr3 Perovskite Nanocrystals Revealed by Femtosecond Transient-Absorption and Single-Dot Luminescence Spectroscopy. *J. Phys. Chem. Lett.* **8,** 1413–1418 (2017).
19. Yu, J. C. *et al.* Improving the Stability and Performance of Perovskite Light-Emitting Diodes by Thermal Annealing Treatment. *Adv. Mater.* **28,** 6906–6913 (2016).
20. Draguta, S. *et al.* Spatially Non-uniform Trap State Densities in Solution-Processed Hybrid Perovskite Thin Films. *J. Phys. Chem. Lett.* **7,** 715–721 (2016).
21. Yang, M. *et al.* Do Grain Boundaries Dominate Non-Radiative Recombination in $CH_3NH_3PbI_3$ Perovskite Thin Films? *Phys. Chem. Chem. Phys.* (2017). doi:10.1039/C6CP08770A

Chapter 5
Conclusion and Future Work

5. 1 Conclusion

The cast-capping method was successfully developed with high potential to be applied in optoelectronics devices. Single-crystal growth for all kind of methylammonium halide perovskites was investigated.

Two-dimensionally growth of single-crystal $MAPbBr_3$ was achieved between glass/glass, glass/mica, DBR/DBR and ITO/ITO substrates. In the glass/glass samples, the (110) face of the single crystals grew two-dimensionally parallel to the substrate surfaces in comparison with the (100) growing plane in the ITO/ITO samples. Being different from $MAPbBr_3$, the limited solubility of $MACl:PbCl_2$ in DMF resulted in small size of single-crystal $MAPbCl_3$. Therefore, DMSO was used instead of DMF, to increase the solubility up to 10% concentration. As a result, the crystals size was increased over several hundreds of μm. In the case of $MAPbI_3$, the cubic single crystals were formed stably at room temperature. With an excess of MAI in the precursor solution, the reverse reaction producing PbI_2 was suppressed, therefore, the crystals size was increased. In addition, the PbI_2 suppressed the single-domain growth even at the $MAI:PbI_2$ ratio up to

4:1. Finally, single-crystal perovskites with mixture halogens were investigated. The crystal lattice constants determined by XRD measurements indicated that the atomic resulted in the lattice constant of mixture-halogen perovskites increased in the order of $d_{MAPbCl3} < d_{MAPbBr(x)Cl(3-x)} < d_{MAPbBr3} < d_{MAPbBr(y)I(3-y)} < d_{MAPbI3}$) in accordance with the increase of ionic radii of halogens (Cl < Br < I).

Subsequently, optically pumped lasing was investigated for single-crystal $MAPbBr_3$ prepared by the cast-capping method. Edge-emitting Fabry-Pérot lasing was observed in the glass/glass samples. This lasing threshold fluence of 12 μJ/cm^2 was much lower than those of ASE reported for the powder layer (350 μJ/cm^2),[1] the WGM for nanoplatelets (30 μJ/cm^2)[2] and the microdisk $MAPbBr_3$ (21 μJ/cm^2)[3] in the previous studies. The Q factor of this F-P resonator was estimated to be 1470, similar with that of 1460 for the $MAPbBr_3$ microdisk lasing.[3] Furthermore, by using DBR/DBR substrates as the casting and capping substrates, vertical-cavity surface emitting lasing was successfully observed in the surface-normal direction. However, their lasing threshold (26 μJ/cm^2) was higher and the Q factor (454) was lower in comparison to those of the edge-emitting F-P laser. Moreover, the edge- and surface-emitting lasers was simultaneously observed in the DBR/DBR samples. The edge-emitting F-P laser was obtained at the threshold of 24 μJ/cm^2 at which the surface emission was still in the spontaneous regime.

Finally, EL was investigated for single-crystal $MAPbBr_3$ in the simple device structure of with ITO/$MAPbBr_3$/ITO prepared by the cast-capping method. Even though without the charge transport layers, EL was observed at very low operation voltage of 2 V. Note that the blinking EL was observed at the crystal edges and corners. Under the applied bias voltages, the injected carriers probably diffused and accumulated at the edges and corners of single-crystal $MAPbBr_3$ where the radiative excitons were predominantly generated. Those excitons contributed to radiative emission through the sub-gap states which was assumed from the red-shifted EL. However, it was considered that chemical defects including uncoordinated Pb atoms and mobile Br ions also allocated at the crystal edges and corners where the excitons were trapped. Therefore, the excitonic emission was quenched by non-radiative recombination at high probability there resulting in the EL blinking.

5. 2 Future work

Improvement of the PeLED performance is still remaining to be addressed in the future work. In PeLEDs, PEDOT:PSS is commonly used as a hole transport layer, however, it causes a non-radiative pathway in perovskite layer.[4,5] On the other side, it is reported that the EQE of PeLED is increased by using long-chain ammonium halides, an excess methylammonium halide and amine passive layer.[6,7] It suggests that those passive layers can coordinate with the Pb atoms resulting in the reduction of non-radiative recombination. As a preliminary investigation in the present study, enhanced PL was observed by pre-coating a MABr layer before cast-capping growth of $MAPbBr_3$ crystals. This pre-coating MABr could passivate the ionic defects, therefore, reduce the non-radiative quenching occurring at the interface between the $MAPbBr_3$ crystal and ITO surface. This passivation technique will lead to improve the performance of PeLEDs prepared by the simple cast-capping method in the future.

After investigating the effects of MABr and PEDOT:PSS on single-crystal $MAPbBr_3$, it is proposed to fabricate ITO/PEDOT:PSS/MABr/$MAPbBr_3$/MABr/TPBi/ITO devices by the cast-capping method as shown in Fig. 5.1. Firstly, PEDOT:PSS and TPBi (as an electron transport layer) are spin-coated on top and bottom ITO substrates, then dried in

vacuum. Then, MABr is spin-coated on these substrates. Finally, the ITO/PEDOT:PSS/MABr and ITO/TPBi/MABr are used as casting and capping substrates to grow single-crystal $MAPbBr_3$ between them. By using TPBi and PEDOT:PSS as electron and hole transport layer, respectively, together with MABr as a passive layer, it is expected to avoid the EL blinking and improve PeLED performance.

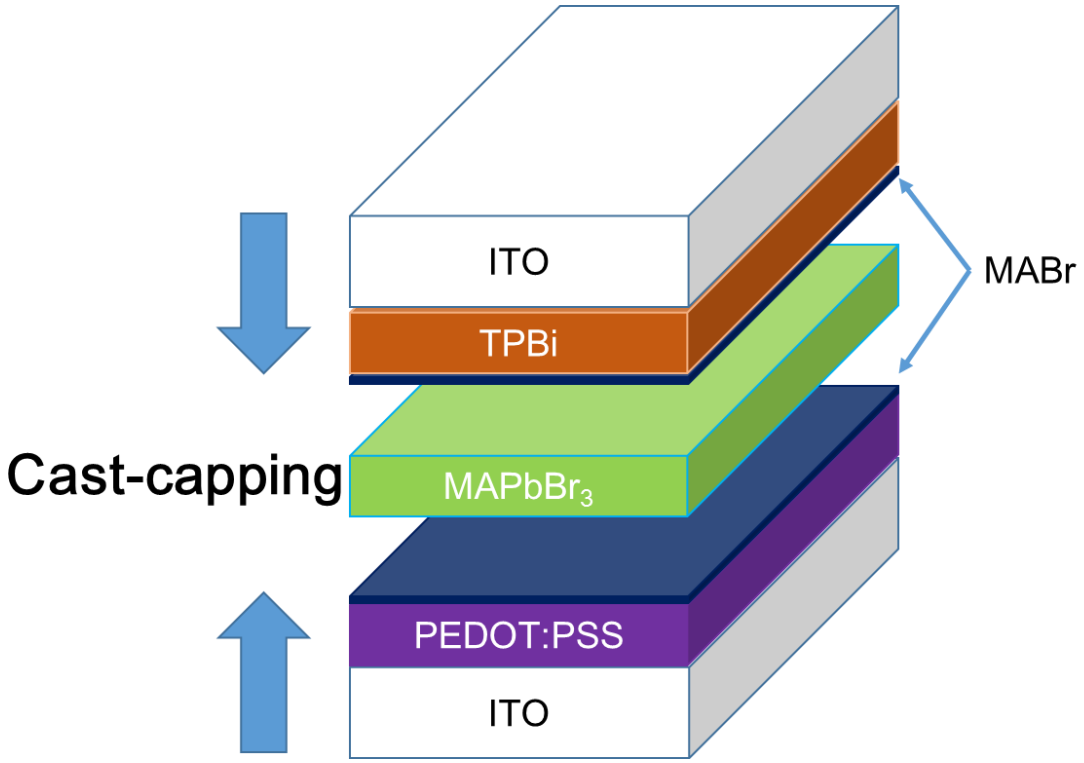

Fig. 5.1: *Schematic of ITO/PEDOT:PSS/MABr/$MAPbBr_3$/MABr/TPBi/ITO device.*

As is well known, one-dimensional (1D) gain media can lase more efficiently than planar (2D) gain media because of low-dimensional confinement of excitons and emitted light. In this sense, a potential device structure is proposed in Fig. 5.2 towards electrically

pumped lasing with single-crystal perovskites in the future. The 1D crystal cavity, for example with a size of 500x10x2 μm^3, can be fabricated by photolithography or laser-etching processing from a large-size single-crystal $MAPbBr_3$ grown by the cast-capping method.

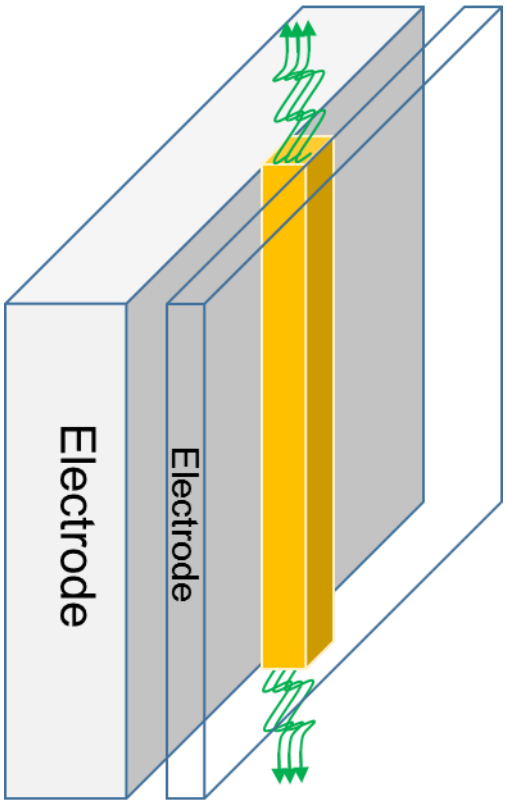

Fig. 5.2: *Schematic of lasing from 1D single-crystal perovskite.*

References

1. Priante, D. *et al.* The recombination mechanisms leading to amplified spontaneous emission at the true-green wavelength in $CH_3NH_3PbBr_3$ perovskites. *Appl. Phys. Lett.* **106,** 81902 (2015).
2. Zhang, Q. *et al.* Room-Temperature Near-Infrared High‐Q Perovskite Whispering-Gallery Planar Nanolasers. *Nano Lett.* **14,** 5995–6001 (2014).
3. Wang, K. *et al.* Unidirectional Lasing Emissions from $CH_3NH_3PbBr_3$ Perovskite Microdisks. *ACS Photonics* **3,** 1125–1130 (2016).
4. DeQuilettes, D. W. *et al.* Impact of microstructure on local carrier lifetime in perovskite solar cells. *Science* **348,** 683–686 (2015).
5. Wen, X. *et al.* Morphology and Carrier Extraction Study of Organic-Inorganic Metal Halide Perovskite by One- and Two-Photon Fluorescence Microscopy. *J. Phys. Chem. Lett.* **5,** 3849–3853 (2014).
6. Xiao, Z. *et al.* Efficient perovskite light-emitting diodes featuring nanometre-sized crystallites. *Nat. Photonics* **11,** 108–115 (2017).
7. Cho, H. *et al.* Overcoming the electroluminescence efficiency limitations of perovskite light-emitting diodes. *Science* **350,** 1222–1225 (2015).

List of Publications

1. Van-Cao Nguyen, Hiroyuki Katsuki, Fumino Sasaki, and Hisao Yanagi, Single-crystal perovskite $CH_3NH_3PbBr_3$ prepared by cast-capping method for light-emitting diodes, *Japanese Journal of Applied Physics* **57**, 04FL10 (2018).

2. Fumio Sasaki, Van-Cao Nguyen, and Hisao Yanagi, Optical pumped lasing and electroluminescence of formamidiniumperovskite semiconductors prepared by the cast-capping method, *Japanese Journal of Applied Physics* **57,** 03EH05 (2018).

3. Van-Cao Nguyen, Hiroyuki Katsuki, Fumino Sasaki, and Hisao Yanagi, Single-crystal perovskites prepared by simple-solution process: Cast-capping method, *Journal of Crystal Growth* **468**, 796-799 (2017).

4. Fumio Sasaki, Ying Zhou, Yoriko Sonoda, Reiko Azumi, Hiroyuki Mochizuki, Van-Cao Nguyen, and Hisao Yanagi, Optically pumped lasing in solution processed perovskite semiconducting materials: Self assembled Fabry-Pérot microcavity, *Japanese Journal of Applied Physics* **56**, 04CL07 (2017).

5. Van-Cao Nguyen, Hiroyuki Katsuki, Fumino Sasaki, and Hisao Yanagi, Optically pumped lasing in single crystals of organometal halide perovskites prepared by cast-capping method, *Applied Physics Letters* **108**, 261105 (2016).

Acknowledgements

Firstly, the author would like to express my sincere gratitude to my supervisor Prof. Hisao Yanagi at Quantum Materials Science Laboratory, Graduate School of Materials Science, Nara Institute of Science and Technology (NAIST) for continuous support of my Ph. D. study and related research, for his patience, motivation, and immense knowledge. His guidance helped me in all the time of experimental and writing not only this thesis but also the publications throughout this study.

My sincere thanks also goes to Associate Prof. Hiroyuki Katsuki at Quantum Materials Science Laboratory, Graduate School of Materials Science, NAIST, and Dr. Fumio Sasaki at Electronics and Photonics Research Institute, National Institute of Advanced Industrial Science and Technology (AIST), for their kind instructions and helpful suggestion.

Besides, I would like to thank the rest of my thesis advisors, Prof. Yukiharu Uraoka, Information Device Science Laboratory, Graduate School of Materials Science, NAIST, and Prof. Youichiro Hosokawa at Bio-Process Engineering Laboratory, Graduate School of Materials Science, NAIST, for their insightful comments, encouragement and helpful suggestions.

The author wishes to express my appreciation to Assistant Prof. Satoshi Tomita and Assistant Prof. Atsushi Ishizumi at Quantum Materials Science Laboratory, Graduate School of Materials Science, NAIST, who provided me an opportunity to access the equipment and research facilities.

I thank all Quantum Materials Science Laboratory members and NAIST staffs, who supported me not only experimental but also daily life during my studies. Without their precious support it would be really hard to focus on study and face the new life in Japan.

The author wishes to thank Associate Prof. Michele Saba, Associate Prof. Francesco Quochi, Dr. Valerio Sarritzu, Mr. Nicola Sestu, Mr. Luca Vellini and Mr. Paolo Usai at Dipartimento di Fisica, Università di Cagliari for their kind experimental guidance, useful suggestions and taking care of my stay at Cagliari University, Italy when I stayed as an internship student.

Last but not least, I would like to thank my wife (Huyen Heo), my parents, my brother, sister and all my friends for supporting me spiritually throughout my study from the beginning.